

# Patient-specific modeling of blood flow in the coronary arteries

Charles A. Taylor<sup>a,\*</sup>, Kersten Petersen<sup>a</sup>, Nan Xiao<sup>a</sup>, Matthew Sinclair<sup>a,b</sup>, Ying Bai<sup>a</sup>,  
Sabrina R. Lynch<sup>a</sup>, Adam UpdePac<sup>a</sup>, Michiel Schaap<sup>a,b</sup>

<sup>a</sup> HeartFlow, Inc., 331 East Evelyn Ave, Mountain View, 94041, CA, USA

<sup>b</sup> Imperial College London, 180 Queen's Gate, London, SW7 2RH, United Kingdom

Available online 6 September 2023

## Abstract

Patient-specific models of blood flow in the coronary arteries have entered clinical practice worldwide to aid in the diagnosis and management of heart disease. This technology leverages modern AI-based image segmentation methods to extract the geometry of the coronary arteries from noninvasive computed tomography volumetric imaging, computational physiology methods to define boundary conditions and computational fluid dynamic techniques to compute coronary artery flow and pressure. The methods described herein have been used to compute the fractional flow reserve (FFR) in the coronary arteries, namely the ratio of pressure in a coronary artery to the reference aortic pressure under conditions of maximum hyperemia induced by the intravenous administration of a vasodilator to mimic increased coronary artery blood flow as occurs during physical activity. The fractional flow reserve derived from coronary computed tomography angiography (CCTA) using patient-specific models of coronary artery blood flow is referred to as  $FFR_{CT}$  and has been validated against invasive measurements using pressure wires in several hundred patients and subsequently evaluated in clinical trials in several thousand patients. Patient-specific models of coronary artery blood flow can be used to predict outcomes of coronary artery revascularization procedures, to identify patients at risk of having a heart attack, and to model tissue perfusion of the microcirculation by coupling with emerging models of cardiac function. This paper provides a state-of-the-art review of computational methods for, and applications of, quantifying blood flow in patient-specific models of the coronary arteries.

© 2023 The Author(s). Published by Elsevier B.V. This is an open access article under the CC BY-NC-ND license (<http://creativecommons.org/licenses/by-nc-nd/4.0/>).

**Keywords:** Patient-specific modeling; Blood flow; Deep learning; Coronary artery

## 1. Introduction

Heart disease is the leading cause of death in the world and is principally caused by atherosclerosis in the coronary arteries which provide blood supply to the heart muscle. Patient-specific computational models of blood flow in the coronary arteries have emerged in recent years as a clinically important technology to aid in the diagnosis and treatment of heart disease [1]. The use of patient-specific models of blood flow in coronary arteries is supported by robust clinical data demonstrating accuracy against direct, invasive measures [2–5] and safety, efficacy and cost-effectiveness when introduced into clinical care [6–9]. In 2021, patient-specific computational methods for modeling coronary artery blood flow were incorporated into the American College of Cardiology and American Heart Association guidelines for the diagnosis and management of heart disease [10].

\* Corresponding author.

E-mail address: [taylorca64@gmail.com](mailto:taylorca64@gmail.com) (C.A. Taylor).

Patient-specific computational models of coronary artery blood flow incorporate mathematical models of blood flow in arteries [11–13]. Any mathematical model of blood flow in the circulation includes at least three elements: first, a geometric description of the anatomic region of interest; second, the mathematical “governing equations” enumerating the physical laws of blood flow within the region of interest; and, third, “boundary conditions” to define physiologic relationships between variables at the boundaries of the region of interest. While the anatomic region of interest and the boundary conditions are unique to each patient and the specific vascular territory, the governing equations describing velocity and pressure are universal and apply in different patients and other arterial beds.

Prior to the advent of three-dimensional medical imaging techniques such as magnetic resonance imaging (MRI) and computed tomography (CT) in the late 20th century, geometric models of arteries were defined based on idealized representations of the arterial tree [14]. Starting in the 1980s, intravenous administration of contrast agents together with magnetic resonance or computed tomography imaging enabled the noninvasive visualization of the arterial tree [15–17]. Taylor et al. described the creation of patient-specific models from three-dimensional medical imaging data [18] which led to the rapid proliferation of image-based models of blood flow [19,20].

Current patient-specific blood flow modeling technology has its origins in efforts to quantify blood flow in arteries using mathematical analysis of fluid dynamics dating back centuries. Early investigators developing mathematical models that quantified relationships between blood flow and pressure had to introduce significant simplifications to the incompressible Navier–Stokes equations. Mathematical models of the circulation can be classified into three categories: (1) the lumped parameter model, (2) one-dimensional wave propagation models, and (3) three-dimensional, numerical models. Chronologically, the development of these models proceeded from lumped-parameter models introduced at the end of the 19th century to the one-dimensional wave propagation equations introduced in the mid-20th century to the three-dimensional finite element methods of the late 20th and early 21st centuries.

Lumped parameter models of the circulation, introduced by Otto Frank, are named as such because spatially-varying properties are lumped into discrete components [21]. For example, the fluid resistance along the length of a vessel is represented as a single resistive element with parameter values derived using an idealized solution to the Navier–Stokes equations, i.e. Poiseuille’s solution for steady, axisymmetric, unidirectional flow in a circular cylindrical model of a blood vessel. While the simplicity of lumped-parameter models enables whole body models of the circulation, it precludes pressure-flow solutions in realistic models of diseased arteries where the requisite mathematical simplifications are invalid. Blood flow in a diseased coronary artery is neither steady, axisymmetric, nor unidirectional and vessel segments are not circular cylinders.

One-dimensional wave propagation models of the circulation are derived by averaging the Navier–Stokes equations over a vessel cross-section, neglecting non-axial components of the velocity vector, assuming the axial velocity profile is the same at all locations along the vessel and in all vessels, and assuming pressure is constant over the vessel cross-section. Fifty years ago, Thomas J.R. Hughes published a seminal paper on the one-dimensional theory of blood flow in elastic vessels including a permeable lateral surface and outflow function to model the distribution of flow through branch vessels [22]. While one-dimensional wave theory assumptions are reasonable for computing flow and pressure in straight and completely healthy segments, they are invalid near side branches, bifurcations or in diseased segments. As a result, one-dimensional wave theory relies on idealized empirical models to approximate pressure losses in stenoses and diseased arteries [23]. Further, loss models for serial lesions or lesions at branches and bifurcations have not been reported — potentially limiting the applicability of one-dimensional wave models to resolve coronary flow and pressure. However, despite these limitations, one-dimensional wave propagation models can be used to solve blood flow in large networks of arteries [24–28].

Three-dimensional models of blood flow employ numerical methods to solve the Navier–Stokes equations governing fluid dynamics. The strengths of this method include the capacity to directly represent the true geometry of the circulation, the full complexity of three-dimensional pulsatile or unsteady flow (including turbulence), and to include complex material models for blood or blood vessels. In the last 25 years three-dimensional numerical methods have become the standard approach for simulating blood flow in arteries [18]. More recent developments have included methods to simulate blood flow in patient-specific models derived from medical imaging data [20], combine three-dimensional models of blood flow in the large arteries with one-dimensional and lumped parameter models of arteries upstream or downstream of the regions of interest [29], and solve the coupled problems of blood flow and vessel wall dynamics [30–35].

Any mathematical model of the circulation is necessarily truncated at some level. Typically, inflow boundary conditions representing blood flow exiting the left ventricle for the systemic circulation or the right ventricle for the pulmonary circulation are prescribed with a velocity profile for three-dimensional simulations or flow rate for one-dimensional wave problems. When using magnetic resonance imaging to image the arterial tree, phase contrast imaging has been used to measure velocity at discrete slices to prescribe boundary conditions [36–40]. Outflow boundary conditions for modeling the portion of the circulation downstream of the region of interest have evolved from specification of zero traction conditions [18,41] to methods to couple a numerical region of interest to reduced order models of the downstream circulation, i.e. multiscale [42] or multidomain methods [29] the latter inspired by the Dirichlet-to-Neumann boundary conditions of Keller and Givoli [43] and the Variational Multiscale methods of Thomas J.R. Hughes [44].

Patient-specific models for coronary blood flow leveraged developments in patient-specific geometric modeling, three-dimensional and one-dimensional wave propagation models and multidomain boundary conditions. Kim et al. described methods to solve the three-dimensional equations of blood flow and vessel wall dynamics in patient-specific models of the coronary circulation [45]. Their models included anatomy of the thoracic aorta and coronary arteries derived from coronary computed tomography angiography (CCTA) data and used lumped parameter models of the heart, systemic circulation and coronary microcirculation. This coupling between three-dimensional models and reduced order models enabled the solution of realistic coronary artery flow and pressure waveforms and formed the foundation for subsequent clinical applications of coronary flow modeling. This work has since been extended to embed patient-specific three-dimensional simulations of blood flow into fully closed-loop lumped-parameter models of the circulation with parameters tuned from patient-specific clinical measurements of blood pressure and cardiac function [46].

In this paper, we describe the development and clinical application of patient-specific modeling of coronary blood flow. In the HeartFlow (HeartFlow, Inc., Mountain View, CA USA) technology described herein and as depicted in Fig. 1, CCTA data acquired for a patient is transmitted through a secure connection from a hospital to an application running on the Amazon Cloud where a combination of image analysis and deep learning algorithms extract the patient’s cardiac anatomy. The results of these algorithms are inspected by a team of trained analysts and corrected when necessary, resulting in a patient-specific geometric model of the aorta, coronary arteries, and left ventricle myocardium. Subsequently, physiological principles are applied to derive patient-specific boundary conditions under simulated maximal hyperemia (mimicking the increased coronary blood flow induced during invasive flow or pressure measurements by the intravenous administration of vasodilators such as adenosine) and compute coronary blood velocity and pressure fields. The primary clinical variable computed in clinical practice to date has been the fractional flow reserve, the local time-averaged blood pressure in the coronary artery divided by the mean aortic pressure under conditions of maximal hyperemia. The fractional flow reserve computed from CCTA data is referred to as  $\text{FFR}_{\text{CT}}$  [1].

The paper is organized as follows. In Section 2 we describe the algorithms and analyst processes to extract the patient specific geometry from the CCTA data. In Sections 3, 4 and 5 we describe respectively geometric domain decomposition, numerical methods and techniques for simulating coronary flow, and how a patient-specific physiological model is applied to derive boundary conditions for coronary blood flow simulation. In Section 6 we describe the application of patient-specific modeling of coronary artery blood flow to the calculation of FFR and summarize the clinical data from a diagnostic perspective. We then discuss the application of these methods to predict risk of heart attacks using patient-specific models and compute changes in FFR subsequent to percutaneous coronary intervention (PCI), i.e. coronary stenting. In Section 7 we describe the future application of patient-specific coronary modeling methods to evaluate coronary microvascular dysfunction (CMD) by extending the image-based computational model to the microcirculation. This approach could enable coupling with emerging methods to model cardiac electromechanical function and cardiac flow in the heart itself. Finally, in Section 8 we close with a brief summary of progress to date.

## 2. Patient-specific anatomy from CCTA

An integral component of HeartFlow’s workflow is the extraction of a patient’s anatomical geometry from their CCTA data. This task is accomplished with an augmented intelligence approach.

Augmented intelligence combines human and machine intelligence to improve the efficiency and accuracy of predictive systems. The objective of augmented intelligence is to harness the interpretative abilities and domain

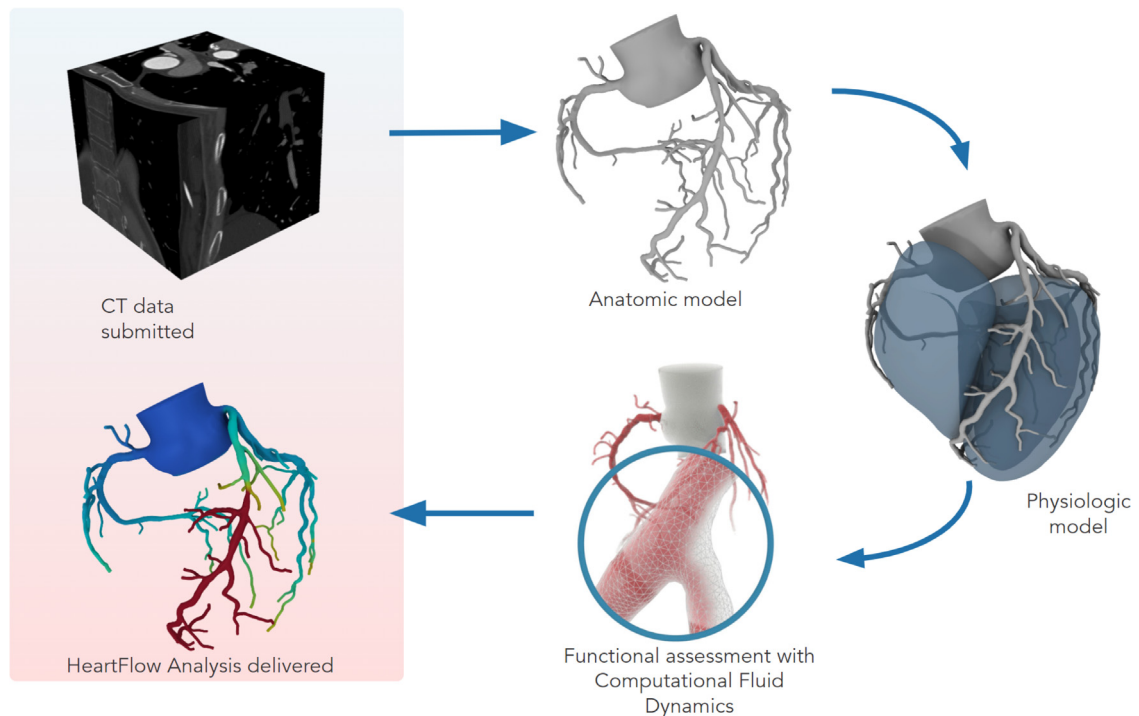


**Fig. 1.** Patient specific modeling of coronary artery blood flow.

expertise of humans where needed while leveraging the speed and computational power of machines where possible. In this human-in-the-loop setup, humans and machines continuously collaborate by refining and augmenting each other through model updates and human intervention [47].

One example of augmented intelligence emerges when artificial intelligence (AI) models analyze images depicting anomalous anatomical features (e.g. aneurysms). In these situations, human intervention becomes crucial to adjust the model's predictions. Human intelligence is characterized by a profound understanding of concepts, enabling humans to interpret and annotate anatomical images with minimal training samples. Humans possess the remarkable ability to extrapolate effectively to unseen image variations, honed through lifelong learning. By incorporating human insights, an AI model can learn from these specific cases and improve its future predictions.

As AI models become more generalized and proficient in handling various scenarios, the reliance on human effort diminishes. This occurs because the models can effectively interpolate between training examples and generate accurate predictions without constant human intervention. Another strength of AI models is their ability to connect information from high-dimensional data, such as multiple 3D images, while humans often work with a limited number of 2D slices extracted from 3D images. By learning from large and information-rich datasets, AI models have the potential to make predictions that are occasionally more accurate than those made by human experts.

Fig. 2 shows the human-in-the-loop process employed by HeartFlow, which we will discuss in more detail in the subsequent sections. CT quality (Section 2.1) is assessed by trained human experts to pick the image with the highest image quality for the structures of interest. Deep learning models extract the large structures of the heart (Section 2.2), the coronary artery centerlines (Section 2.3), and the lumen (Section 2.4) from the CCTA image. The outputs of each of these stages are reviewed and corrected by human experts to ensure that the final anatomical model is ready for precise physiological modeling and disease assessment. At present, the human review and correction of anatomic models requires approximately 30–45 min per case depending on disease burden and image quality whereas compute time for the various steps is typically less than 15 min. Finally, this human-in-the-loop paradigm generates user-corrected datasets that can be utilized to train more accurate models, resulting in more efficient processing by human experts.

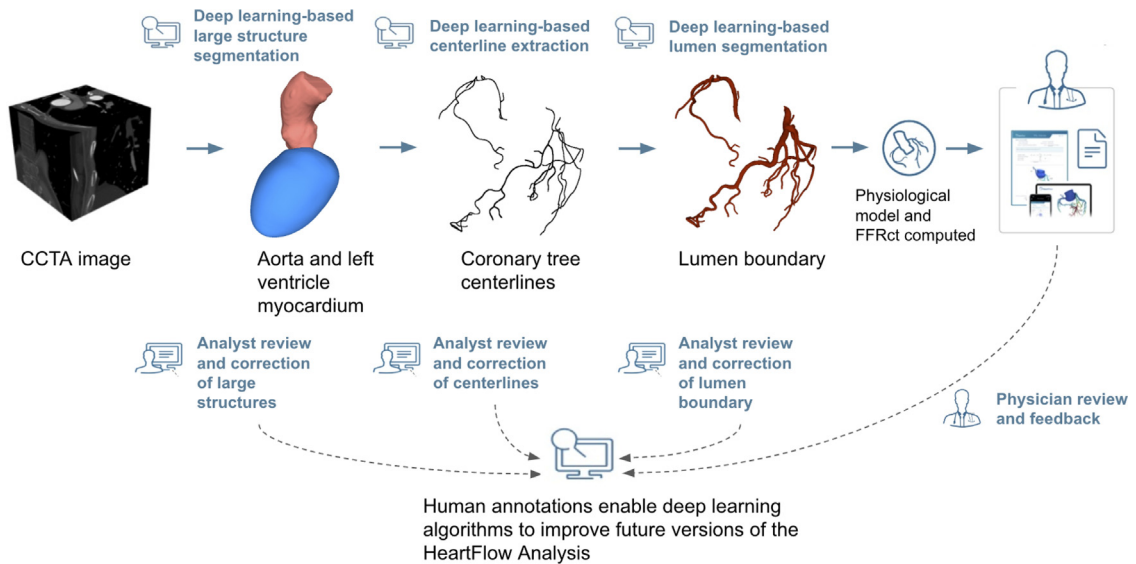


**Fig. 2.** HeartFlow processes CCTA images with a human-in-the-loop approach. Human review and correction improve the accuracy of deep learning-based segmentations, which may serve as training data for future training of deep learning models. More accurate automated predictions may reduce the effort for future manual intervention and thereby increase the accuracy, reproducibility, and efficiency of the overall geometry extraction.

## 2.1. CT quality

A CCTA scan often results in multiple 3D volumes of image data. The different volumes can represent different phases of the cardiac cycle and different ways of reconstructing the 3D volumetric data from the raw measurements. After HeartFlow receives the 3D CCTA volumes from the hospital or imaging center, trained human experts use advanced visualization tools to determine which of the 3D volumes is most suited to extract the patient's coronary geometry and they determine if the image quality is sufficient for extracting an accurate representation of the patient's coronary geometry. For this, the coronary arteries are assessed at every location along the coronary artery tree to determine if it contains locally sufficient image information to reliably and accurately extract the coronary lumen boundary. After determining that the quality of the image is good enough, the analysts continue with the inspection of the outputs of the anatomy extraction deep learning methods.

## 2.2. Large structures

The human heart contains four chambers consisting of two ventricles and two atria. The left atrium (LA) receives oxygenated blood from the pulmonary circulation and feeds into the left ventricle (LV), which pumps oxygenated blood to the systemic circulation. The right atrium (RA) receives deoxygenated blood from the systemic circulation and feeds into the right ventricle (RV), which pumps deoxygenated blood to the pulmonary circulation. The heart muscle, or myocardium, contracts and relaxes to pump blood through the heart and around the systemic and pulmonary circulatory systems. The LV myocardium is particularly thick as it is responsible for pumping blood to the systemic circulation, and as such has the highest oxygen demand of the chambers, and receives the majority of the blood supplied to the heart tissue via the coronary arteries.

It is important to accurately segment the LV myocardium in order to estimate the total resting blood flow received by the coronary circulation and to appropriately distribute the blood flow amongst the coronary arteries (see Section 5). Additionally, segmentation of the ascending aorta, which carries blood from the left ventricle to the body, and identification of the aortic valve and coronary ostia are key to modeling accurate coronary blood flow.

A common approach for extracting the geometry of the cardiac chambers from 3D CCTA image data involves a segmentation model, optionally followed by a shape fitting model. Deep learning-based voxel-wise prediction



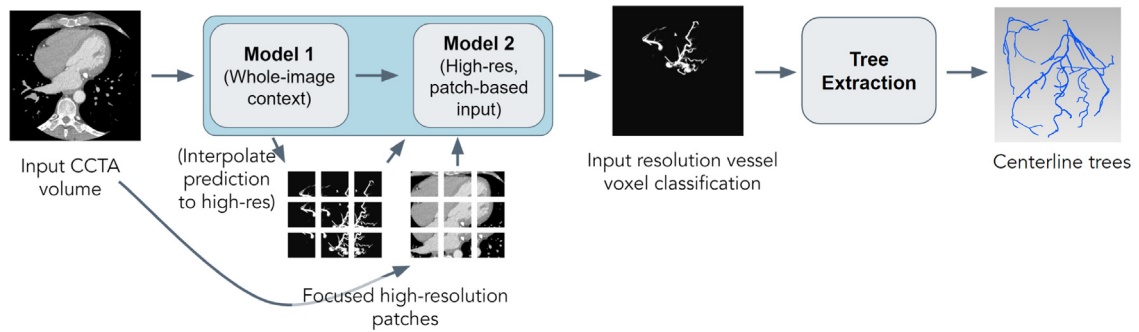


**Fig. 3.** Deep learning based centerline extraction using a 3D U-Net Cascade model [49].

models, such as the U-net [48] and models with similar such encoder–decoder architectures, produce state-of-the-art performance on a range of 3D medical image segmentation tasks [49]. In addition to a voxel-wise segmentation, an atlas-based registration method can be used to ensure a consistent topology and mitigate noisy voxel-wise predictions e.g. anatomically inaccurate spurious segmentations or holes [50].

Other structures such as the ascending aorta and the landmark coordinates of the aortic valve and the coronary ostia can also be accurately predicted with a U-net model, where landmark coordinates can be extracted from predicted (3D) Gaussian heat maps [51]. The outputs of our large structures models include the LV myocardium, the ascending aorta, and the landmark coordinates of the aortic valve and coronary ostia. These structures are visually assessed and corrected where necessary, and provide inputs to downstream tasks including centerlines extraction, lumen segmentation, and our physiological model.

### 2.3. Centerlines

Coronary centerline extraction is a fundamental and crucial task in modeling the geometry of coronary trees. The goal is to detect and extract the coronary vessel tree topology from a given 3D CCTA image. Extracted centerlines can be used as inputs for lumen or plaque segmentation and efficient manual navigation and inspection of data.

Traditional centerline extraction approaches typically rely on hand-crafted image features [52] and adopt tracking or region-growing based methods, which are error-prone and susceptible to local variations caused by imaging noise and artifacts, loss of opacification, or disease. Modern deep learning based methods usually first perform voxel-based vessel segmentation using a state-of-the-art model for 3D medical image segmentation [49,53], and then extract centerline trees as the skeletons of the vessel segmentation masks. For image segmentation, one popular and efficient machine learning framework is the cascaded classifier, which use a series of classifiers to integrate multi-scale contextual information for image segmentation [54–56]. The output of each classifier is used as the contextual information for the next classifier in the series. The 3D U-Net cascade [49] is an example of this framework, in which the first U-Net operates on downsampled images to detect target object and produce a coarse resolution segmentation, and the second U-Net aims to refine the segmentation at full image resolution. We adopted a similar approach as in [49] and trained a cascaded model using a diverse and large dataset (more than four thousand CCTA images). With minimal post-processing to remove noise and gaps, the vessel segmentation masks can be used to detect vessel outlets and define a cost function for extracting centered paths between vessel tree roots and outlets [57]. Finally the extracted paths can be merged into centerline trees (see Fig. 3).

To ensure accurate modeling of all cases including outliers with low image quality or rare diseases, analysts can inspect and edit the automatically extracted centerlines using a suite of semi-auto tools in a special-purpose visualization workstation. Operations such as adding vessels or refining centerline locations can be performed efficiently by placing a few anchor points. User corrections can be leveraged in future model training to further improve robustness to variations in imaging protocols and patient anatomy.

### 2.4. Lumen segmentation

Accurate segmentation of vascular structures plays a crucial role in improving the diagnosis, treatment, and surgical planning of vascular disease. A notable example is the need for precise lumen segmentation to calculate

coronary blood flow and pressure fields, which are vital for assessing the hemodynamic significance of lesions. For this application, vessels are preferably segmented with sub-voxel accuracy given that vessel resistance to blood flow is inversely proportional to the fourth power of the vessel diameter (according to Poiseuille's law) and computational predictions of coronary flow and pressure are especially sensitive to geometry [58].

There are several challenges associated with achieving detailed vessel segmentation. First, the input images typically consist of around  $512^3$  voxels, while vessels may only be few voxels wide. Second, the curvature and branching patterns of vessels can vary significantly among patients. Third, the appearance and geometry of vessels may be influenced by disease patterns, such as the presence of soft, mixed, or calcified plaques, as well as anatomical abnormalities like myocardial bridging. Lastly, the interpretation of images may be hindered by imaging noise, partial volume effects, blooming, misregistration artifacts, or other image artifacts.

In recent years, vessel segmentation has been a prominent area of research, resulting in numerous proposed approaches [59]. Here, we will focus on lumen segmentation methods developed at HeartFlow, which have demonstrated high accuracy when compared to optical coherence tomography (OCT) measurements — the reference standard for quantifying luminal and outer wall geometry [60]. HeartFlow's lumen segmentation approach consists of three main steps, as illustrated in Fig. 4. First, a technique called straightened curved planar reformation (sCPR) [61] is utilized to create a stacked representation of approximately orthogonal cross-sectional frames along the vessel's centerline. This process optimizes the orientation of the frames to minimize distortion when the centerlines takes abrupt turns.

Second, a deep learning-based regression model named DeepLumen is employed. This model falls under the category of generalized cylinder models and aims to predict the distance from the centerline to the lumen boundary in 32 equiangular directions at every centerline location. To achieve this, a fixed-sized sub-volume is extracted from the sCPR representation at each vessel path location, with an inter-frame spacing of 0.25 mm. DeepLumen was designed as a regression model for two main reasons. First, adopting a voxel-level classification approach could potentially give rise to topological problems, such as the emergence of spurious or disconnected label regions. Second, considering that the image resolution supplied to DeepLumen is set at  $0.25 \text{ mm}^3$ , this resolution might prove insufficient for effectively modeling small blood vessels, potentially leading to the creation of jagged segmentation borders. In contrast, utilizing regression techniques yields a continuous and connected lumen surface, allowing for the possibility of achieving theoretically limitless precision in representing the location of the lumen's boundary.

Finally, a surface reconstruction algorithm is utilized to construct a water-tight mesh based on the regressed distances around all the vessels of a given case.

DeepLumen was trained on more than six thousand CCTA cases randomly selected from routine clinical use of HeartFlow's FFR<sub>CT</sub> product. These cases spanned the spectrum of disease severity, falling into one of three categories: low, moderate, or high. Within the low disease severity group, constituting approximately 40% of cases, resided those instances characterized by the presence of standalone simple plaques with clear lumen boundaries, or the absence of plaque. Moderate disease severity claimed another 40%, where multiple standalone lesions and focal stenoses were observed. This category occasionally encompasses a single region of complex plaque. The remaining 20% displayed high disease severity, which features a large amount of plaque, particularly calcified mixed plaque or other complex plaque affecting multiple or all vessels and bifurcations.

The DeepLumen architecture is fully convolutional and utilizes leaky rectified linear units as activation functions. The network consists of eight  $3 \times 3$  convolutional layers with 32 kernels each, as well as two fully connected layers with 64 and 128 kernels, respectively. For hyper-parameter optimization and training, approximately 4 million training samples were randomly sampled from the cross-sectional stacks. During training, various forms of image intensity augmentation, such as scaling and additive Gaussian noise, were applied to increase the model's robustness.

### 3. Geometric domain definition

After a 3D model is accurately and robustly segmented from the input image data, there are additional steps required to prepare a 3D domain for fluid simulation. These steps can vary depending on the numerical method being used to solve the fluids equations. We will primarily discuss the preparation of a domain through meshing for the finite element method. We will also explain some of the important features of meshes for blood flow simulation, as well as simplifications of the geometry and methods to facilitate quicker solve times such as a hybrid 1D/3D approach.

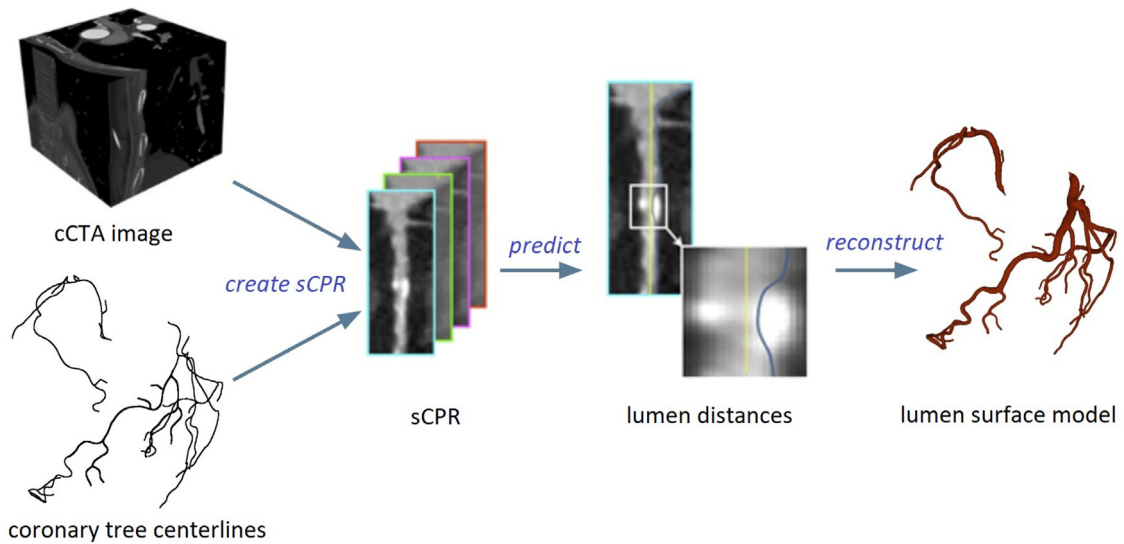


**Fig. 4.** Overview of HeartFlow's lumen segmentation: sCPR representation is generated for views rotated around the centerline. For illustration purposes, four sCPR angle directions are shown, even though 32 are used in the algorithm. As a next step, the distance from the medial axis of each slice (yellow) to the lumen boundary (blue) is predicted. Finally, the lumen surface model is constructed from the predicted lumen boundary points. (For interpretation of the references to color in this figure legend, the reader is referred to the web version of this article.)

In general, mesh generation consists of taking an input 3D geometry and discretizing it into the combination of adjacent smaller pieces, typically called elements. The elements provide smaller, finite locations on which the equations of interest can be solved. The size and shape of the elements are very important in order to achieve a converged and accurate solution. A way to guarantee this is to generate a fine mesh with very small elements; however, this will make the mesh quite large and thus, take longer to solve. Typically, a mesh refinement study is performed where varying levels of mesh sizes are compared to a simple solution on a very fine mesh to find the optimal balance between solution accuracy and solution speed. In addition to obtaining a mesh size that provides both speed and accuracy, there are other important mesh options or features that can aid in obtaining a quick and accurate solution.

Local mesh refinement and coarsening are features that help in obtaining that balance between speed and accuracy. Depending on the 3D geometry, there may be locations in which the solution is changing more or less rapidly; thus, local mesh refinement/coarsening can be applied to match the mesh to the specifics of the domain. For example, for coronary geometries, a coarser mesh can be applied to the interior of the aorta where the solution is changing less rapidly than in a tight stenosis, where a finer mesh size can be applied (Fig. 5B,C).

Mesh adaptation is similar to local mesh refinement and coarsening, but instead of identifying locations and prescribing sizes manually, aspects of the solution are used to understand how the solution is changing and locally refine and coarsen the mesh accordingly [62]. Typically, the Hessian of the solution or the second directional derivative is used as an approximation of the error to obtain an optimal size (Fig. 5D,E).

Boundary layer meshing is an important feature for fluid simulations with a no slip boundary condition on the surface where the solution changes rapidly from zero velocity at the wall to the speed of the fluid [63]. Thin, elongated elements are layered along the surface in order to pack more points perpendicular to the surface, capture the changing solution, and prevent the simulation from diverging (Fig. 5F).

Hybrid modeling and simulation is discussed further in Section 4. Briefly, in some locations of the geometry such as healthy distal coronary vessels, a reduced order simulation can provide an accurate enough solution, and a full, 3D mesh is not required. In these instances, the 3D domain can be removed or truncated and attached to the 1D representation of the geometry. Again, this works to increase the speed of the simulation while still maintaining an accurate solution, see Fig. 6.

Reduced order models (ROM) are also discussed further in Section 4. For reduced order methods including 0D, 1D, and 2D methods, a full 3D domain is not required. Like in hybrid modeling, a lesser representation of the



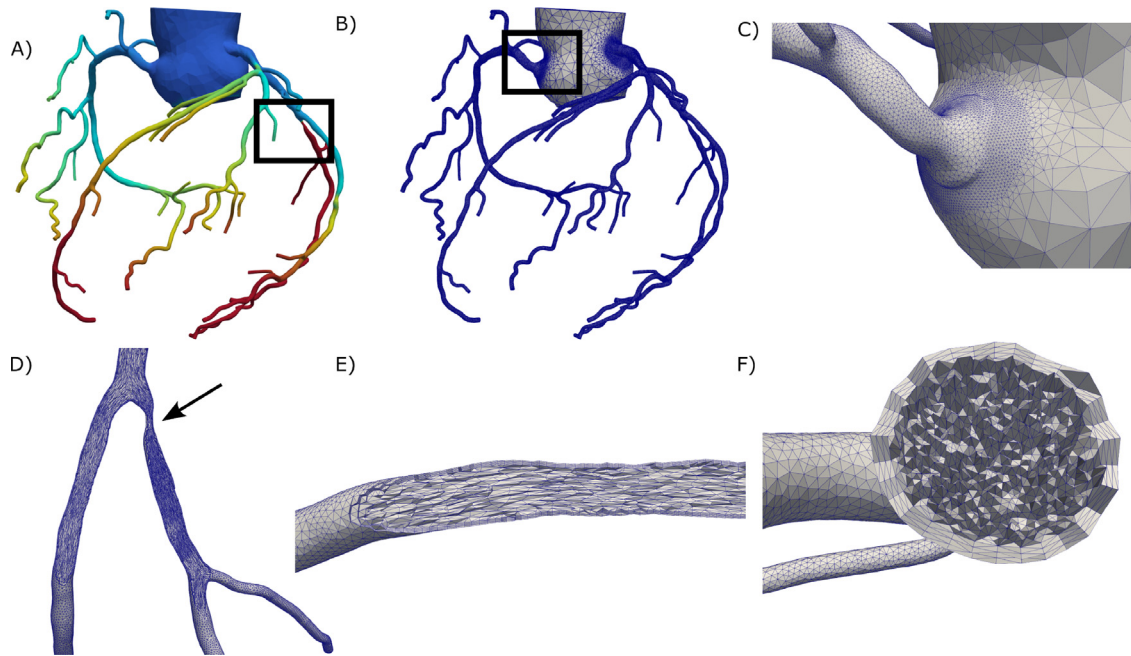


**Fig. 5.** (A) Example HeartFlow analysis with stenosis highlighted in the black box; (B) example finite element mesh with ostium refinement highlighted in the black box; (C) mesh refinement at the right ostium; (D) mesh refinement post stenosis (black arrow); (E) alignment of mesh dimensions with flow; and (F) mesh boundary layers. Mesh generation was performed using the MeshSim software (Simmetrix, Inc., Clifton Park, NY USA).

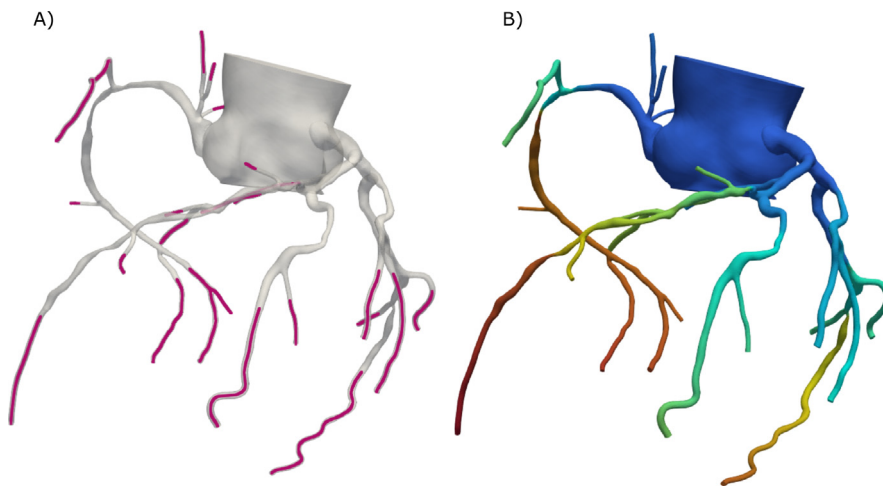


**Fig. 6.** (A) Hybrid domain, 1D domain is highlighted in red. (B)  $FFR_{CT}$  solution. (For interpretation of the references to color in this figure legend, the reader is referred to the web version of this article.)

domain is sufficient as long as approximations of the geometry are accurate. For example, in a 1D simulation, the geometry can be represented through radii or diameter values along centerline points, and should contain enough points to capture changes in the geometry necessary for understanding the fluid dynamics.

For any simulation, it is essential to ensure that the domain and domain preparation is adequate for the mathematical modeling being used and the simulation being performed. The mathematical modeling is explained further in the subsequent sections. For the complex, 3D mesh generation techniques described above, there are

various commercial packages that provide these functionalities. MeshSim (Simmetrix, Clifton Park, NY USA) was used for mesh generation for the examples shown herein [64].

#### 4. 3D, Hybrid and ROM methods

In this section, we describe the numerical methods used to simulate blood flow in the coronary arteries. In particular we focus on the three-dimensional (3D) and reduced-order formulations, which are appropriate for high-fidelity simulations and rapid turn-around respectively. We also describe the coupling of 3D and reduced-order modeling of coronary flow to leverage the advantages of both approaches.

##### 4.1. 3D formulation

The 3D formulation for blood flow in the large vessels of the cardiovascular system such as the epicardial coronary arteries can be approximated as an incompressible Newtonian fluid. Consider a domain  $\Omega \in \mathcal{R}^{n_{sd}}$  where  $n_{sd}$  is the number of spatial dimensions. The boundary  $\Gamma$  of the spatial domain  $\Omega$  is split into a Dirichlet partition  $\Gamma_g$  and a Neumann partition  $\Gamma_h$  such that  $\Gamma = \partial\Omega = \Gamma_g \cup \Gamma_h$  and  $\Gamma_g \cap \Gamma_h = \emptyset$ . The 3D equations governing the dynamics of an incompressible Newtonian fluid consist of the momentum balance and mass conservation equations subject to suitable boundary and initial conditions:

$$\begin{aligned} \rho \vec{u}_{,t} + \rho \vec{u} \cdot \nabla \vec{u} &= -\nabla p + \nabla \cdot \boldsymbol{\tau} + \vec{f} \\ \nabla \cdot \vec{u} &= 0 \end{aligned}$$

where  $\boldsymbol{\tau} = 2\mu \mathbf{D}$  with  $\mathbf{D} = \frac{1}{2}(\nabla \vec{u} + \nabla \vec{u}^T)$

(1)

$$\begin{aligned} \vec{u}(\vec{x}, t) &= \vec{g}(\vec{x}, t), & \vec{x} &\in \Gamma_g \\ \vec{\tau} \vec{n} &= [-p\mathbf{I} + \boldsymbol{\tau}] \vec{n} = \vec{h}(\vec{u}, p, \vec{x}, t), & \vec{x} &\in \Gamma_h \\ \vec{u}(\vec{x}, 0) &= \vec{u}_0(\vec{x}), \quad p(\vec{x}, 0) = p_0(\vec{x}) & \vec{x} &\in \Omega \end{aligned}$$

The unknowns are the fluid velocity  $\vec{u} = (u_x, u_y, u_z)$  and pressure  $p$ . The density  $\rho$  and the viscosity  $\mu$  of the fluid are assumed to be constant, and  $\vec{f}$  is the external body force.  $\vec{g}$  defines the imposed velocities on the Dirichlet boundary and  $\vec{h}$  defines the imposed traction on the Neumann boundary.  $\vec{u}_0$  is the initial velocity field and  $p_0$  is the initial pressure. For modeling blood flow in the coronary vessels, the Dirichlet boundary typically contains the luminal boundary of the vessel on which  $\vec{g} = 0$  and possibly the artificially truncated inflow face, and the Neumann boundaries are the artificially truncated outflow faces.

For the weak formulation, the trial solution and weighting function spaces for the semi-discrete formulation of the momentum balance and continuity equations are defined as follows:

$$\begin{aligned} \mathcal{S} &= \{\vec{u} \mid \vec{u}(\cdot, t) \in H^1(\Omega)^{n_{sd}}, \quad t \in [0, T], \quad \vec{u}(\cdot, t) = \vec{g} \text{ on } \Gamma_g\} \\ \mathcal{W} &= \{\vec{w} \mid \vec{w}(\cdot, t) \in H^1(\Omega)^{n_{sd}}, \quad t \in [0, T], \quad \vec{w}(\cdot, t) = \vec{0} \text{ on } \Gamma_g\} \\ \mathcal{P} &= \{p \mid p(\cdot, t) \in H^1(\Omega), \quad t \in [0, T]\} \end{aligned}$$
(2)

Here,  $H^1(\Omega)$  represents the Sobolev space of functions which are square-integrable in  $\Omega$  and whose first derivatives are also square-integrable.  $L^2[0, T]$  represents the Hilbert space of functions which are square-integrable in time  $[0, T]$ .  $n_{sd}$  is the number of spatial dimensions. We assume  $n_{sd}$  is 3.  $\vec{g}$  is the assigned Dirichlet boundary condition (i.e. the imposed velocities, which are zero on the lumen wall). The weak formulation can then be written as follows: find  $\vec{u} \in \mathcal{S}$  and  $p \in \mathcal{P}$  such that for any  $\vec{w} \in \mathcal{W}$  and  $q \in \mathcal{P}$  the following is satisfied:

$$\begin{aligned} B(\vec{w}, q; \vec{u}, p) &= 0 \text{ where} \\ B(\vec{w}, q; \vec{u}, p) &= \int_{\Omega} \{\vec{w} \cdot (\rho \vec{u}_{,t} + \rho \vec{u} \cdot \nabla \vec{u} - \vec{f}) + \nabla \vec{w} : (-p\mathbf{I} + \boldsymbol{\tau})\} d\Omega \\ &\quad - \int_{\Omega} \nabla q \cdot \vec{u} d\Omega - \int_{\Gamma_h} \vec{w} \cdot (-p\mathbf{I} + \boldsymbol{\tau}) \vec{n} ds + \int_{\Gamma} q \vec{u} \cdot \vec{n} ds \end{aligned}$$
(3)

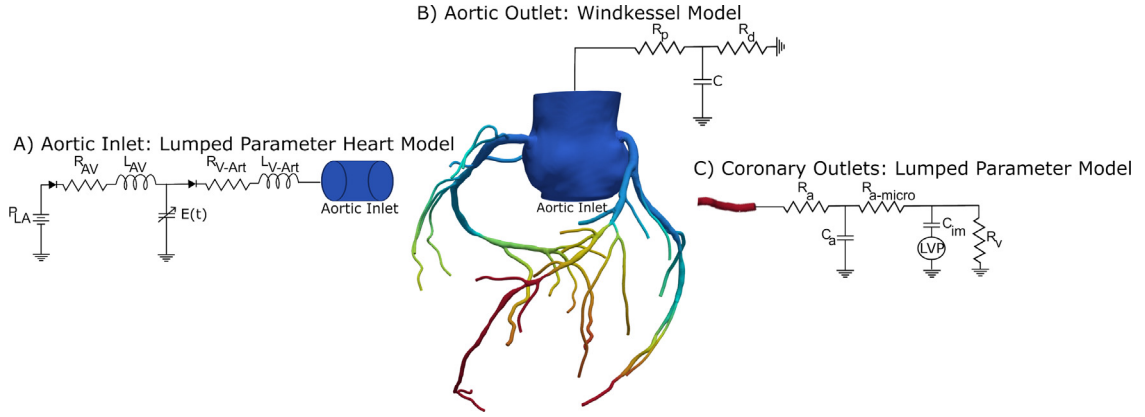


Fig. 7. Geometric domain with boundary conditions.

The Neumann boundary consists of the artificially truncated outlets and potentially the inlet(s) of the 3D domain; for these boundaries, we define operators to approximate the fluid stress and velocity as follows:

$$\begin{aligned} (-p\mathbf{I} + \boldsymbol{\tau})|_{\Gamma_h} &\approx [\mathbf{M}_m(\vec{u}, p) + \mathbf{H}_m]_{\Gamma_h} \\ \vec{u}|_{\Gamma_h} &\approx [\vec{M}_c(\vec{u}, p) + \vec{H}_c]_{\Gamma_h} \end{aligned} \quad (4)$$

These operators generalize the relationships between the velocity and pressure fields at the Neumann boundaries, allowing the coupling of resistance, impedance, lumped-parameter, or more complex reduced-order fluid dynamic models to approximate the effects of the surrounding vasculature on the 3D domain [29,45], see Fig. 7.

An additional term for ‘backflow stabilization’ at the Neumann boundaries is considered to mitigate flow instabilities, which can occur during the transient initial portion of the solution process. This additional term in the weak formulation describes an inward traction that is applied only for parts of the boundary that experience inward velocities, relative to the surface normal [65]:

$$B(\vec{w}, q; \vec{u}, p) = B(\vec{w}, q; \vec{u}, p) - \frac{\beta}{2} \int_{\Gamma_h} \rho \vec{w} \cdot \vec{u} (\vec{u} \cdot \vec{n} - |\vec{u} \cdot \vec{n}|) ds = 0 \quad (5)$$

The traction at the lumen wall may be used to understand the hemodynamic forces that are acting on vulnerable regions of the vessel, such as areas containing atherosclerotic plaques. After obtaining the solution to the original weak formulation (Eq. (3)), we may reinterpret the entire boundary  $\partial\Omega$  as a Neumann boundary, split into the inlet(s)  $\Gamma_{in}$ , outlets  $\Gamma_{out}$ , and vessel lumen wall  $\Gamma_{wall}$  such that  $\partial\Omega = \Gamma_{in} \cup \Gamma_{out} \cup \Gamma_{wall}$ . Assuming that the lumen wall and inlet boundaries were originally Dirichlet boundaries and the outlets remain Neumann boundaries, it is possible to obtain a variationally-consistent boundary traction using the solved pressure ( $\bar{p}$ ), velocity ( $\vec{u}$ ), and weighting function space  $\mathcal{W}^\perp$ , the orthogonal complement of  $\mathcal{W}$ , by solving for  $\vec{t}^f$  which contains the wall traction of interest:

$$\begin{aligned} \int_{\Gamma_{wall} \cup \Gamma_{in}} \vec{w} \cdot \vec{t}^f ds &= \int_{\Omega} \{ \vec{w} \cdot (\rho \vec{u}_{,t} + \rho \vec{u} \cdot \nabla \vec{u} - \vec{f}) + \nabla \vec{w} : (-p\mathbf{I} + \boldsymbol{\tau}) \} d\Omega \\ &\quad - \int_{\Gamma_{out}} \vec{w} \cdot (-p\mathbf{I} + \boldsymbol{\tau}) \vec{n} \quad \forall \vec{w} \in \mathcal{W}^\perp \end{aligned} \quad (6)$$

To approximate the solution of the weak formulation (Eq. (3)), we employ a robust stabilized semi-discrete finite element method formulation [18,66,67] based on the ideas originally introduced by Hughes and colleagues [68,69]. Equal order interpolation for the velocity and pressure fields (P1-P1) using piecewise-linear polynomials is computationally practical, but it is well known that this choice generates an unstable numerical scheme. This along with the advective instability of the standard Galerkin method requires the use of pressure and momentum stabilization, together with additional terms to address the lack of momentum conservation due to the momentum stabilization in the continuity equation [18].

#### 4.2. Reduced-order model formulation

While the full 3D formulation is useful for producing high-fidelity solutions that reveal the interaction between the hemodynamic quantities of interest and the complex anatomical shapes of vessels, particularly in the presence of disease, a reduced-order formulation which enables rapid solution turnaround may often be more practical for answering the most relevant clinical questions, such as the calculation of  $\text{FFR}_{\text{CT}}$ . Here we describe the one-dimensional (1D) formulation [22] for modeling blood flow, where the mass and momentum balance equations are derived from the Navier–Stokes equations, assuming that flow is uni-directional. We consider a straight cylindrical segment of a fixed length and we assume that all the fluid dynamic quantities are axially symmetric. In this setting,  $z$  is the coordinate along which the axis of the vessel is oriented and  $A$  is the cross-sectional area of the vessel. The  $z$  component of the velocity field is the dominant component and pressure is assumed to be constant across each axial cross-section. Viscous effects are non-negligible only near the wall boundary, which is assumed to be impermeable. With these assumptions, integration of the Navier–Stokes equations over the axial cross-section yields the following equations:

$$\begin{aligned}\frac{\partial A}{\partial t} + \frac{\partial Q}{\partial z} &= 0 \\ \frac{\partial Q}{\partial t} + \frac{\partial}{\partial z} \left( \alpha \frac{Q^2}{A} \right) + \frac{A}{\rho} \frac{\partial P}{\partial z} + K_R \frac{Q}{A} &= 0 \\ A(z, t) &= \int_{S(z, t)} dz \\ Q(z, t) &= \int_{S(z, t)} u_z(x, y, z, t) dx dy \\ P(z, t) &= \frac{1}{A(z, t)} \int_{S(z, t)} p(x, y, z, t) dx dy\end{aligned}\quad (7)$$

where  $Q$  is the flow rate through each axial cross-section, obtained by integrating the axial velocity component  $u_z$  over the cross-section  $S(z, t)$ ,  $P$  is the pressure at each cross-section, obtained by integrating the pressure field  $p(x, y, z, t)$ , and  $\rho$  is the blood density.  $K_R$  is a resistance parameter related to the blood viscosity. The coefficient  $\alpha$  [27] is the momentum correction coefficient defined as  $\alpha = \frac{\int_S u_z^2 d\gamma}{A \bar{u}^2} = \frac{\int_S s^2 d\gamma}{A}$  where  $s(x; \zeta)$  is a profile function describing the shape of the velocity profile in the  $z$  direction. For a typical polynomial profile law  $s(x) = \zeta^{-1}(\zeta + 2)(1 - x^\zeta)$  with the polynomial degree  $\zeta > 0$ ,  $\alpha = (\zeta + 2)(\zeta + 1)^{-1}$ . It is common to assume parabolic velocity profiles in the axial direction, hence  $\zeta = 2$  and  $\alpha = 4/3$ , and the value of the resistance parameter is then  $K_R = 8\pi\nu$ , where  $\nu$  is the kinematic viscosity of blood. For the calculation of  $\text{FFR}_{\text{CT}}$  at a clinically-relevant level of accuracy, it is sufficient in practice to omit the time-dependent component of blood flow; in the steady state limit, assuming that the quantities are invariant with time, integrating over a specific length interval  $L$ , and making the assumption that the quantities are constant across the segment yields an expression for the pressure drop:

$$-\Delta P = (aQ + b)LQ \quad (8)$$

$$a = -\frac{\rho\alpha}{A^3} \frac{\partial A}{\partial z}, \quad b = \frac{\rho K_R}{A^2} \quad (9)$$

Note that the term  $aQ + b$  can be seen as a flow-dependent resistance coefficient per-unit-length. Continuing in this simplified setting, the coronary vessel tree is represented by a graph of connected cylindrical segments. If we define  $\mathbf{p}$  as a finite-dimensional vector containing the pressures between successive cylindrical segments (i.e. defined at the nodes of the tree) and  $\mathbf{q}$  as the vector of steady-state flow rates within each cylindrical segment (i.e. defined on the edges of the graph), then we can write a system of equations representing the discretized version of the 1D model as  $\mathbf{A}^T \mathbf{C}(\mathbf{q}) \mathbf{A} \mathbf{p} = \mathbf{f}$ , where the matrix  $\mathbf{A}$  is the connectivity matrix, where row  $j$  corresponds to an edge  $j$  in the one-dimensional network, and within each row, the  $i$ th entry is either 1 or  $-1$  if the node  $i$  belongs to edge  $j$  and 0 otherwise.  $\mathbf{C}(\mathbf{q})$  is the flow-dependent conductance matrix encoding the inverse of the flow-dependent resistance values for each edge in the network.  $\mathbf{f}$  is the vector of nodal flow sums, where most entries are zero except for those corresponding to the nodal flow sources, e.g. the inflow or outflow nodes where flow is prescribed. This nonlinear system of equations can then be solved for the nodal pressure  $\mathbf{p}$ , which will in turn provide the flow rates via  $\mathbf{q} = \mathbf{C}(\mathbf{q}) \mathbf{A} \mathbf{p}$ .

#### 4.2.1. Enhancements to the 1D vessel resistances

While the basic one-dimensional formulation typically enables good approximations to the 3D solutions in the context of computing pressure losses in healthy and very mildly-diseased coronary vessels, the viscous losses incurred by blood flow through narrow stenoses or complex junctions that are naturally captured in the 3D setting may not be accurately modeled in 1D without additional modifications to the vessel resistances [70–75]. In the case of severe disease, high vessel tortuosity, or the presence of certain junctions, physics-based or empirically-derived models may be used to augment the basic vessel resistances derived from the 1D formulation. Moreover, with the availability of 3D solutions from a large number of vessels and patients, it is possible to define an additional flow-dependent conductance that is learned with a suitable ML model [75] from the 3D simulated pressure losses  $C_{ML} = m(Q, C, \mathbf{y}; \theta)$ , parameterized by  $\theta$ , where  $\mathbf{y}$  is a feature vector summarizing the local anatomical vessel shape, and  $C$  is the purely physics-based conductance value. This ML model trained to correct the basic 1D formulation may be applied locally to the areas of the coronary tree that exhibit the largest error between the basic 1D and 3D formulations.

#### 4.2.2. Coupled 3D and 1D formulation

The 1D model is coupled to the solver using a Neumann boundary condition on the inflow/outflow faces of the 3D domain. We can write an expression for the pressure coming from the 1D model as a function of the velocities on the 3D coupled face (indexed by  $i$  and denoted by  $\Gamma_h^i$ ):  $P_i = \text{ROM}(Q_i)$ , where  $Q_i$  is the flow rate obtained by integrating the normal component of the velocity vectors on the surface. At each of the coupled Neumann boundaries, a boundary condition is applied that embeds the contribution of the reduced-order model into the weak formulation of the 3D problem:

$$\int_{\Gamma_h^i} \bar{\mathbf{w}} \cdot (-p\mathbf{I} + \boldsymbol{\tau}) \bar{\mathbf{n}} ds = \int_{\Gamma_h^i} \text{ROM}(Q_i) \bar{\mathbf{w}} \cdot \bar{\mathbf{n}} ds \quad (10)$$

#### 4.3. Solver applications to PCI planning

The FFR<sub>CT</sub> Planner is a novel application that allows for virtual stenting of coronary stenoses and prediction of post-PCI FFR<sub>CT</sub>. This tool enables real-time geometry modifications to a patient-specific lumen segmentation of the coronary vessel tree, and subsequently calculates a real time update to FFR<sub>CT</sub>. The main goal of the FFR<sub>CT</sub> Planner is to enable a real-time update to FFR<sub>CT</sub> due to changes in lumen geometry without compromising accuracy. Predicted post-PCI FFR<sub>CT</sub> is calculated using a novel solver referred to as the Delta-solver.

The Delta-solver is a reduced order model that leverages pre-computed solutions to re-compute FFR<sub>CT</sub> after modifications to lumen geometry. The FFR<sub>CT</sub> Delta-solver uses at least three solver results as inputs: (1) a hyperemic solution using the original patient geometry, (2) a super-hyperemic (“superemic”) solution using the original patient geometry, and (3) a hyperemic solution on an idealized model (i.e. without modeled stenoses). The “superemic” condition is defined for the purposes of this application as a 40% reduction of the hyperemic boundary resistances. From these solutions, the algorithm takes the input model, including both the geometry (radius) and function (flow, pressure). A predictor corrector algorithm that converges upon reaching a specified error or maximum number of iterations is used to update flowrates and pressure in the modified geometry [76]. An example of the prediction of post-PCI FFR<sub>CT</sub> results is shown in Fig. 8.

### 5. Physiologic model and boundary conditions

Appropriate numerical values for the boundary conditions are required to solve for coronary blood flow as the connection between the computational domain and the rest of the cardiovascular system must be modeled in a physiologically realistic way. It is critical to model patient-specific physiological conditions to obtain solutions that are accurate compared to real-world measurements. For the computation of FFR<sub>CT</sub> in particular, since invasively-measured FFR is a time-averaged quantity, a steady state computational model can approximate FFR reasonably well without degrading the accuracy. The so-called physiological model is the algorithm that provides the blood flow simulation with appropriate numerical values for the boundary conditions to enable an accurate representation of patient-specific coronary physiology. In the FFR<sub>CT</sub> setting, the primary function of the physiological model is the computation of the coronary boundary resistances during simulated hyperemia. These resistances represent the



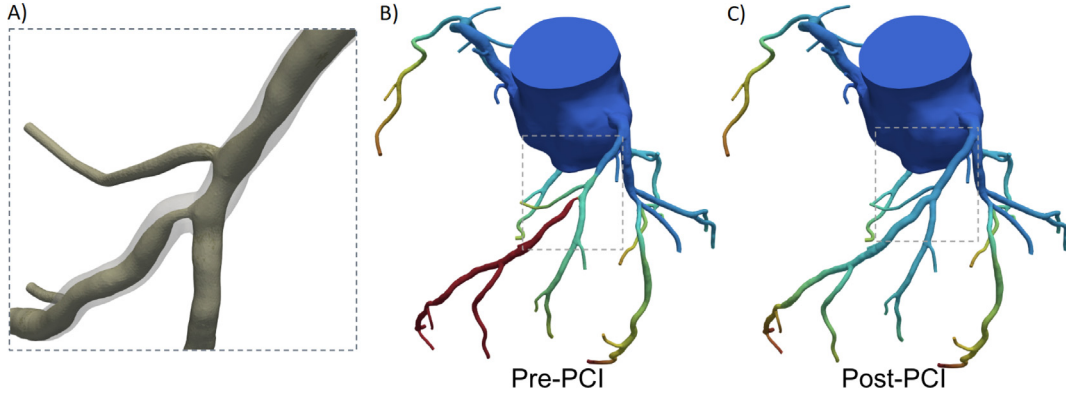


**Fig. 8.** (A) The pre-PCI and predicted post-PCI geometry overlaid, (B) The FFR<sub>CT</sub> solution prior to geometry modification, (C) the FFR<sub>CT</sub> solution after geometry modification to remove areas of stenosis.

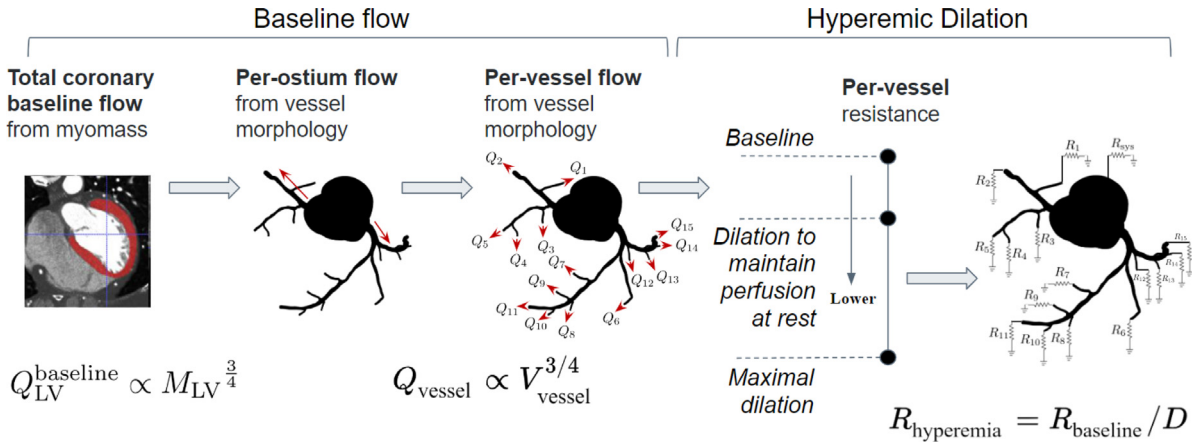


**Fig. 9.** Steps in deriving boundary conditions.

resistances of the downstream microvessels that are not directly observed in the imaging data; they are estimated using information from the observable anatomy in the image, namely, the left ventricle geometry and mass, and the epicardial coronary artery geometry. The algorithm that encodes this process is described below and depicted in Fig. 9.

The first step is the estimation of the total coronary baseline flow, which must satisfy the flow demands of the myocardium at an idealized physiological state of rest. Blood flow to the heart is regulated to meet the oxygen consumption of the myocardial tissue. This is represented in the model by an allometric relationship between total coronary baseline flow and the myocardial mass:  $Q_{baseline} = cM_{myo}^{\frac{3}{4}}$  [77], where the scaling coefficient  $c$  is a parameter adjusted to reproduce clinically-measured values of per-unit-tissue flow. The total coronary baseline flow is then divided among the coronary ostia using morphometric scaling laws that relate vascular volume to flow:  $Q_{subtree} \propto V_{subtree}^{\frac{3}{4}}$  [77]. This process must account for the absence of anatomical information about the right ventricle and atria and the knowledge that certain coronary vessels may perfuse multiple heart chambers. For example, in patients with right-dominant coronary arteries, the right coronary artery branches into vessels that perfuse both the left ventricle (LV) and right ventricle. The per-ostium flows are then distributed to each of the coronary vessel outlets again using a flow-volume scaling law. At each branch junction, the flow to the branches is proportional to the total volume of the downstream vessels, and the baseline flows are assigned to each vessel in the modeled coronary tree following a top-down recursive process.

The resulting per-vessel baseline flows are then used to calculate an idealized healthy per-outlet resting microvascular resistance, where it is assumed that the pressure loss along the epicardial coronary arteries is

negligible. This idealized resting resistance represents the state of the resistance vessels downstream assuming they are fully healthy and that the large epicardial vessels are fully healthy. This is in contrast to the actual state of the coronaries at rest, where significant pressure losses may occur in the large arteries due to the presence of atherosclerotic disease. Then, the per-outlet hyperemic resistances are computed by scaling the idealized resting resistances with a dilation capacity factor representing the effect of adenosine on reducing the peripheral resistance of the coronary microcirculation [78]. The choice of using an idealized resting resistance as the baseline enables realistic modeling of the phenomenon whereby the microvasculature dilates to preserve baseline flow in the presence of mild to severe disease [79]. Since the total dilation capacity is fixed with respect to the idealized resting state, the amount of hyperemic flow that can be achieved is limited by the severity of disease in the large epicardial vessels; this approach also quantifies the amount of total dilation capacity that must be “used up” at rest due to the presence of epicardial disease: it is possible to compute the actual resting resistances given the required resting flow demand and the state of disease in the modeled vessels, and the comparison between these actual resting resistances to the idealized minimal resistances yields the fraction of the dilatory capacity that has been used. For example, if the epicardial coronary artery is fully healthy, the microvasculature remains in an undilated state as the pressure gradient from aorta to myocardium is minimal, achieving the assigned baseline flow. If there is a focal stenosis or diffuse narrowing along the epicardial coronary artery, the microvasculature is dilated to compensate for the pressure loss occurring at the epicardial coronary arteries. As the disease progresses, the pressure loss within the epicardial coronary arteries increases such that the microvasculature must dilate further to compensate for the pressure loss.

A primary goal for the physiological model is robustness to geometric variation. Specifically, the outlet resistances generated from the physiological model should be relatively invariant to small perturbations in the anatomical input data, which may result from image noise, variability between human analysts, or minor changes in the geometric algorithms. This consideration largely motivated the choice of a top-down recursive vascular-volume based approach to flow-distribution as opposed to a bottom-up approach using outlet areas [80]. As the relative distribution of the total baseline flow into the individual vessel is largely determined by vascular volume, it is important then to consider a definition of vascular volume that is not directly derived from the actual coronary geometry, but rather an idealized geometry that is robust to areas of focal narrowing.

During the simulation, the outlet resistances are adjusted on-the-fly as a function of the distal coronary pressures and aortic pressure in order to model passive mechanisms that respond to pressure changes. Specifically, this resistance adjustment serves as a simple autoregulatory model to allow the simulated pressures to remain relatively unchanged over a wider range of aortic pressures. This is to allow the model to mimic clinical observations that invasively-measured FFR is relatively independent of the aortic pressure.

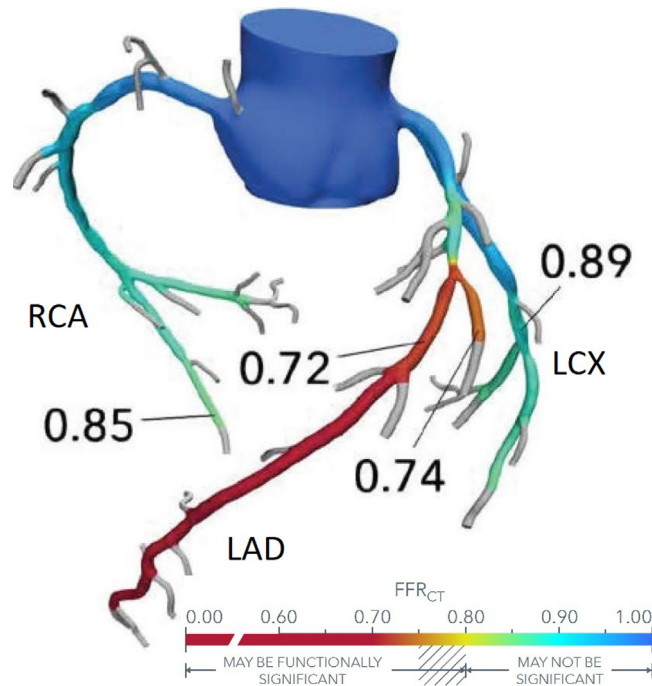
## 6. Application to coronary artery disease diagnosis and treatment planning

Fig. 10 displays an example result for a patient with functionally significant disease in the left anterior descending (LAD) coronary artery.

The diagnostic performance of  $\text{FFR}_{\text{CT}}$  has been evaluated in four clinical trials using measured FFR as the reference standard and blinded core laboratory control. In each study  $\text{FFR}_{\text{CT}}$  showed good correlation to FFR and demonstrated significant improvement in diagnostic accuracy and specificity compared to CCTA alone.

The first clinical trial to evaluate  $\text{FFR}_{\text{CT}}$  technology was the DISCOVER-FLOW trial which included 103 patients and 159 vessels from 4 sites in the U.S., Europe and Asia [2].  $\text{FFR}_{\text{CT}}$  improved diagnostic accuracy compared to CCTA (84% vs. 59%) with a twofold improvement in specificity (84% vs. 40%) and no difference in sensitivity (87% vs. 91%).  $\text{FFR}_{\text{CT}}$  showed significant improvement in discrimination of ischemia (defined by invasively measured  $\text{FFR} \leq 0.80$ ) with an increase in the area under the curve (AUC) of the receiver operating characteristics curve when compared to CCTA, 0.90 versus 0.75 ( $p < 0.001$ ).

The second clinical trial, the DeFACTO study, was comprised of 252 patients with 407 vessels directly interrogated by FFR. The diagnostic accuracy of  $\text{FFR}_{\text{CT}}$  was higher than CCTA stenosis (73 vs. 64%), as was the specificity (54% vs. 42%) with similar high sensitivity (90% vs. 84%).  $\text{FFR}_{\text{CT}}$  demonstrated superior per-patient and per-vessel discrimination of ischemia when compared to CCTA, with AUCs of 0.81 versus 0.68 ( $p < 0.001$ ) and 0.81 versus 0.75 ( $p < 0.001$ ), respectively. In patients with an intermediate stenosis ranging from 30% to 70%, there was more than a twofold increase in sensitivity, from 37% for CCTA to 82% for  $\text{FFR}_{\text{CT}}$ , with no loss of specificity [81].



**Fig. 10.** Example of  $FFR_{CT}$  results. Disease in the Left Anterior Descending Coronary artery (LAD) would be deemed to be functionally significant as it falls below the threshold value of 0.80. In contrast, the Right Coronary Artery (RCA) and the Left Circumflex (LCX) coronary artery have  $FFR_{CT}$  values above 0.80 and would be deemed to be functionally non-significant.

The third clinical trial to evaluate the diagnostic accuracy of  $FFR_{CT}$ , the NXT trial, investigated the diagnostic performance of  $FFR_{CT}$  in 254 patients and 484 vessels [4]. The software used incorporated refinements in image processing methods and physiologic modeling, using information derived from previously studied patients in prior trials. In addition, the lessons learned from prior clinical trials were incorporated into the NXT trial protocol with image quality assessment by the  $FFR_{CT}$  core lab and mandated adherence to image acquisition guidelines with respect to the use of Sublingual Nitroglycerine (NTG) and beta-blockers. In NXT, nitrates were administered in 99.6% and beta-blockers were used in 78% of patients. The per-vessel accuracy and specificity to identify arteries with invasively measured  $FFR \leq 0.80$  were significantly higher for  $FFR_{CT}$  (86% and 86%) than for CCTA (65% and 60%) ( $p < 0.001$ ). Sensitivity was unchanged at 83% for CCTA and 84% for  $FFR_{CT}$ .  $FFR_{CT}$  also demonstrated superior per-patient and per-vessel discrimination of ischemia when compared to CCTA, with AUCs of 0.90 versus 0.81 ( $p < 0.001$ ) and 0.93 versus 0.79 ( $p < 0.0001$ ), respectively.  $FFR_{CT}$  demonstrated a good correlation with FFR with a Pearson's correlation coefficient of 0.82 ( $p < 0.001$ ). For patients with intermediate stenosis severity (30%–70%), per-patient sensitivity and specificity to identify arteries that caused myocardial ischemia were 85% and 79% for  $FFR_{CT}$  as compared to 93% and 32% for CCTA ( $p = \text{N.S.}$  for sensitivity,  $p < 0.0001$  for specificity).

The fourth and most recent trial to evaluate the diagnostic accuracy of  $FFR_{CT}$ , the PACIFIC trial, investigated the diagnostic performance of  $FFR_{CT}$  in 208 patients and 505 vessels with suspected coronary artery disease, who underwent CCTA, Single Photon Emission Computed Tomography (SPECT), Positron Emission Tomography (PET), and invasive FFR measurements. The diagnostic performance of these methods were compared using invasively-measured FFR in 505 vessels as the reference standard.  $FFR_{CT}$  showed a diagnostic accuracy, sensitivity, and specificity of 87%, 90%, and 86% on a per-vessel basis. The area under the receiver-operating characteristic curve (AUC) for identification of invasively-measured FFR positive lesions was significantly greater for  $FFR_{CT}$  (0.94) in comparison with CCTA (0.81), SPECT (0.70), PET (AUC 0.87) with  $p < 0.01$  for all three comparisons.

With the diagnostic accuracy of patient-specific models of coronary artery blood flow established, it remained to be shown that patients could be properly managed using information obtained from the computational models. Specifically, it remained to be proven that patients with a negative test result could be safely deferred from

subsequent invasive testing and that patients with a positive test result would be more likely to be treated when taken to the cardiac catheterization laboratory for further invasive assessment. The PLATFORM trial examined a standard patient management strategy compared to CCTA plus FFR<sub>CT</sub> guided management in 580 patients with planned invasive coronary testing [6]. The CCTA plus selective FFR<sub>CT</sub> strategy was associated with a significantly lower rate of subsequent angiography showing no obstructive CAD, low rates of clinical outcomes, similar quality of life, and significant cost savings achieved by deferring invasive testing in many patients. The ADVANCE registry further evaluated the use of FFR<sub>CT</sub> in clinical practice in 5083 patients and demonstrated a very low adverse event rate, less subsequent invasive testing or treatment in patients with a negative FFR<sub>CT</sub> compared with patients with abnormal FFR<sub>CT</sub> values [82,83]. Recently, the PRECISE clinical trial randomized 2103 patients to either a “precision” strategy including CCTA and FFR<sub>CT</sub> vs. traditional diagnostic testing [84]. The primary endpoint of the clinical trial was evaluated at 1 year and was a composite of death, non-fatal myocardial infarction, or an unnecessary invasive cardiac catheterization (defined as an invasive test where no obstructive coronary artery disease was identified). The precision strategy using patient-specific modeling of coronary blood flow showed a 70% reduction in the primary endpoint as compared with the traditional testing pathway. Specifically, the precision strategy was 78% more likely to identify patients in need of revascularization while reducing the need for subsequent invasive diagnostic testing [85].

Finally, as a result of the clinical evidence supporting the use of patient-specific modeling of coronary blood flow, the American College of Cardiology and American Heart Association guidelines for the diagnosis and management of heart disease recommend FFR<sub>CT</sub> to determine the functional significance of coronary artery disease ranging from a 40% to 90% diameter stenosis identified on CCTA [10].

Patient-specific computational models of blood flow may also provide important information for predicting which atherosclerotic plaques are at risk of rupturing and causing heart attacks. The EMERALD clinical trial [86] studied 72 patients that had CCTA acquired between 1 month and 2 years before a subsequent heart attack where the culprit lesion was identifiable during the cardiac catheterization used to treat them. Anatomic and plaque characteristics were extracted from the CCTA data and patient-specific models of coronary blood flow were performed to compute FFR<sub>CT</sub> as well as time-averaged wall shear stress. A key finding was that the trans-lesional gradient of FFR<sub>CT</sub> was the single best predictor of plaque rupture causing the subsequent heart attacks. Furthermore, predictive models combining plaque characteristics and hemodynamic variables outperformed those based on diameter stenosis alone [87]. The recently published DESTINY study further supports the use of patient-specific models of coronary artery blood flow for predicting risk of heart attacks [88].

Patient-specific computational models of blood flow can also be leveraged for treatment planning whereby alternate therapeutic interventions can be simulated and used to predict likely changes in coronary blood flow and pressure. Sankaran et al. described a real-time simulation technology using reduced order models to compute changes in fractional flow reserve subsequent to geometric modifications to a computational model reflecting removal of diseased regions as occurs during percutaneous coronary interventions (PCI), i.e. stenting [89]. This technology has been cleared by the U.S. FDA for clinical use and was recently tested in a diagnostic accuracy trial comparing predicted post-PCI FFR results to measured values [90]. A motorized pullback system was used to measure FFR values enabling a detailed comparison to the CCTA-extracted geometry and simulation at 97,402 matched locations at a 0.1 mm spacing along the centerlines. The mean difference between predicted post-PCI FFR<sub>CT</sub> and invasively-measured post-PCI FFR values was 0.01 with a standard deviation of 0.05. A recent consensus document highlighted the importance of leveraging patient-specific modeling of coronary artery blood flow for procedural planning [91]. Both this technology to predict post-PCI FFR as well as other CCTA-extracted information has the power to help guide coronary catheterizations [92,93]. Ultimately, cardiac bypass grafting procedures could also be planned using CCTA-based patient-specific methods [94].

## 7. Future applications

### 7.1. Fluid–structure coupling for coronary flow and vessel biomechanics

Personalized risk assessment of coronary plaque vulnerability is an exciting opportunity that can help doctors make well-informed decisions about treatment and interventions. Clinicians may one day use techniques that segment atherosclerotic plaques from CCTA images, estimate their material properties, and conduct a biomechanical simulation to assess the risk of material failure, plaque rupture and heart attacks. Deep learning-based segmentation models for the outer wall of coronary vessels and precise estimation of plaque composites are active areas of

research [95]. HeartFlow's DeepPlaque technology was developed as an extension of the DeepLumen algorithm in Section 2.4, and was recently evaluated in the REVEALPLAQUE study with measurements from intravascular ultrasound (IVUS). A total of 432 lesions were assessed in 237 patients and strong correlations for total plaque volume, as well as calcified and non-calcified plaque volumes [96] compared to IVUS data have been reported. Previous work has also examined the material properties of these plaque composites, which can be used to understand how the outer wall behaves under blood-flow induced stress. With these advancements, biomechanical simulations are on the horizon that assess the risk of coronary artery plaque rupture using mechanistic methods to evaluate a patient's risk and enable timely interventions to reduce adverse cardiovascular events.

## 7.2. Coronary microvascular dysfunction

Beyond the assessment of coronary artery disease (CAD), coronary microvascular dysfunction (CMD) is an increasingly recognized therapeutic target, with a prevalence amongst the stable chest pain population of up to 50% [97]. Both the 2021 joint AHA/ACC Guidelines [10] and 2019 ESC Guidelines [98] include clinical pathways to identify and treat CMD in the INOCA (ischemia with no obstructive coronary arteries) population. For the *non-invasive* evaluation of the microcirculation, the AHA/ACC Guidelines [10] recommend the use of quantitative perfusion CMR or PET, for patients with non-obstructive CAD (NOCAD). However, the definition of NOCAD in the guidelines is <50% diameter stenosis, where such stenoses can still cause a hemodynamically significant reduction in coronary flow [99,100]. The presence of both hemodynamically significant epicardial disease as well as CMD can confound the direct interpretation of quantitative perfusion images. For the *invasive* evaluation of the microcirculation, the AHA/ACC Guidelines [10] recommends the measurement of coronary flow reserve (CFR) [79], or (hyperemic) index of microvascular resistance (IMR) [101]. Each of these has its own limitations for assessing CMD, including the impact of both epicardial and microvascular disease on the measurement of CFR, and the variability of IMR measured in different territories and across patients due to its dependence on total flow in the target vessel. To circumvent issues observed with existing metrics for CMD diagnosis, microvascular resistance reserve (MRR) has more recently been proposed [102]. Unlike CFR, MRR provides an isolated measure of microvascular function, even in the presence of coronary artery disease. Also unlike IMR, MRR is a measure of the vasodilatory capacity of the coronary microcirculation. In a recent study using 1481 patients from the ILIAS registry [103], MRR was shown to have independent prognostic value in predicting Major Adverse Coronary Events (MACE) even amongst patients with functionally significant epicardial disease ( $FFR < 0.75$ ), whereas IMR and CFR did not.

Computational modeling of coronary blood flow presents a unique and valuable opportunity to estimate MRR non-invasively. Non-invasive estimation of MRR would be of particular clinical interest given that there are no invasive *treatments* for patients with CMD (unlike for CAD), meaning patients without CAD (but suspected CMD) could avoid invasive procedures, whether diagnostic or remedial, altogether. In recent work, methods have been proposed for extending the 3D epicardial tree geometry obtained from cCTA to the scale of the microcirculation with the generation of distal synthetic trees [104–106]. These extended vascular geometries have subsequently been used in coupled models of reduced order Navier–Stokes flow in the coronary arteries and Darcy flow to simulate distribution of blood flow throughout the myocardium [105–107]. By obtaining true patient flow at rest and hyperemia to parameterize total flow in such simulations (e.g. from quantitative perfusion imaging), it becomes possible to accurately quantify microvascular resistance at rest and hyperemia, enabling the computation of  $MRR_{CT}$  as a non-invasive surrogate to MRR.

## 7.3. Coupled multi-physics models

Patient-specific modeling of coronary artery blood flow including the computation of perfusion in the myocardial tissue offers the opportunity to reproduce or leverage cardiac perfusion data available from many modalities. Such models could also be coupled to comprehensive whole human heart electromechanics and cardiac fluid dynamics models [108–110]. This could enable the further integration with other imaging modalities including magnetic resonance imaging or stress echocardiography for examining contractile function or electrocardiograms to measure electrical activity (EKG). Indeed, in the future, patient-specific computational models may enable the complete diagnosis of heart disease from atherosclerosis in a coronary artery to the clinical manifestations of reduced



myocardial blood flow impairing cardiac contraction, electrical function and the pumping capacity of the heart itself. Physicians could then interact with these patient-specific models to evaluate the prognosis of the patient and simulate the benefit of medical treatments and procedures to optimize heart health. Ultimately, simulation-based methods for modeling complete cardiac function could transform healthcare from the current paradigm based on diagnostic and empirical data to one where outcomes are predicted and optimized for individual patients as envisioned at the start of the era of patient-specific modeling of blood flow [18,111].

## 8. Conclusions and outlook

It is perhaps counter-intuitive that for identification of coronary artery disease, a mathematical model that simulates blood flow based purely on anatomic data as input ( $\text{FFR}_{\text{CT}}$ ) could be more accurate for assessing the functional significance of disease than the direct interpretation of anatomic data itself (e.g. stenosis severity in CCTA) or via direct interpretation of measured perfusion deficits. The simple explanation for this paradox is that modern image segmentation algorithms including deep learning can be more anatomically consistent and accurate than visual interpretation by a human and that there is much more data contained in the CCTA than just the percent stenosis of a lesion. By constructing a complete anatomic model of the coronary arteries visible in CCTA data using modern deep learning image segmentation techniques and leveraging established physiologic principles and the physical laws of fluid dynamics, accurate predictions of the functional significance of coronary artery lesions can be attained. In prospective, multicenter clinical trials, by combining anatomy, physiology and fluid mechanics,  $\text{FFR}_{\text{CT}}$  has demonstrated a superior diagnostic performance compared to FFR than that attainable by anatomy alone, or perfusion techniques such as PET and SPECT. This accuracy is expected to further improve by continuous adaptation of the software facilitated by data obtained from clinical trials and clinical usage. Furthermore, large prospective clinical trials have demonstrated that patient-specific computational models of coronary artery blood flow can be used to safely defer further invasive testing in patients with a negative test and identify those patients most likely to benefit from revascularization treatments of coronary artery disease. This technology has also demonstrated the ability to predict outcomes of interventions using mechanistic, image-based computer models of blood flow — enabling physicians to design improved therapies for individual patients that optimize coronary blood flow, tissue perfusion and cardiac function. As we look forward to this new era of medicine one must acknowledge this future has been made possible by the tremendous advances in computational mechanics made by Thomas J.R. Hughes over the last 50 years.

## Declaration of competing interest

The authors declare the following financial interests/personal relationships which may be considered as potential competing interests: Charles A. Taylor reports a relationship with HeartFlow Inc that includes: board membership, employment, and equity or stocks. Kersten Petersen, Nan Xiao, Matthew Sinclair, Ying Bai, Sabrina R. Lynch, Adam UpdePac, Michiel Schaap report a relationship with HeartFlow Inc that includes: employment.

## Data availability

The data that has been used is confidential.

## References

- [1] C.A. Taylor, T.A. Fonte, J.K. Min, Computational fluid dynamics applied to cardiac computed tomography for noninvasive quantification of fractional flow reserve: scientific basis, *J. Am. Coll. Cardiol.* 61 (22) (2013) 2233–2241.
- [2] B.-K. Koo, A. Erglis, J.-H. Doh, D.V. Daniels, S. Jegere, H.-S. Kim, A. Dunning, T. DeFrance, A. Lansky, J. Leipsic, et al., Diagnosis of ischemia-causing coronary stenoses by noninvasive fractional flow reserve computed from coronary computed tomographic angiograms: results from the prospective multicenter DISCOVER-FLOW (diagnosis of ischemia-causing stenoses obtained via noninvasive fractional flow reserve) study, *J. Am. Coll. Cardiol.* 58 (19) (2011) 1989–1997.
- [3] J.K. Min, J. Leipsic, M.J. Pencina, D.S. Berman, B.-K. Koo, C. Van Mieghem, A. Erglis, F.Y. Lin, A.M. Dunning, P. Apruzzese, et al., Diagnostic accuracy of fractional flow reserve from anatomic CT angiography, *JAMA* 308 (12) (2012) 1237–1245.
- [4] B.L. Nørgaard, J. Leipsic, S. Gaur, S. Seneviratne, B.S. Ko, H. Ito, J.M. Jensen, L. Mauri, B. De Bruyne, H. Bezerra, et al., Diagnostic performance of noninvasive fractional flow reserve derived from coronary computed tomography angiography in suspected coronary artery disease: the NXT trial (analysis of coronary blood flow using CT angiography: Next steps), *J. Am. Coll. Cardiol.* 63 (12) (2014) 1145–1155.

- [5] R.S. Driessen, I. Danad, W.J. Stuijzand, P.G. Raijmakers, S.P. Schumacher, P.A. Van Diemen, J.A. Leipsic, J. Knuuti, S.R. Underwood, P.M. van de Ven, et al., Comparison of coronary computed tomography angiography, fractional flow reserve, and perfusion imaging for ischemia diagnosis, *J. Am. Coll. Cardiol.* 73 (2) (2019) 161–173.
- [6] P.S. Douglas, B. De Bruyne, G. Pontone, M.R. Patel, B.L. Norgaard, R.A. Byrne, N. Curzen, I. Purcell, M. Gutberlet, G. Rioufol, et al., 1-year outcomes of FFRCT-guided care in patients with suspected coronary disease: the PLATFORM study, *J. Am. Coll. Cardiol.* 68 (5) (2016) 435–445.
- [7] B. Nørgaard, C. Terkelsen, O. Mathiassen, E. Grove, H. Bøtker, E. Parner, et al., Clinical outcomes using coronary CT angiography and FFRCT-guided management of stable chest pain patients, *J. Am. Coll. Cardiol.* 72 (18) (2018) 2123–2134.
- [8] M.A. Hlatky, B. De Bruyne, G. Pontone, M.R. Patel, B.L. Norgaard, R.A. Byrne, N. Curzen, I. Purcell, M. Gutberlet, G. Rioufol, et al., Quality-of-life and economic outcomes of assessing fractional flow reserve with computed tomography angiography: PLATFORM, *J. Am. Coll. Cardiol.* 66 (21) (2015) 2315–2323.
- [9] N. Curzen, Z. Nicholas, B. Stuart, S. Wilding, K. Hill, J. Shambrook, Z. Emlinton, D. Ball, C. Barrett, L. Johnson, et al., Fractional flow reserve derived from computed tomography coronary angiography in the assessment and management of stable chest pain: the FORECAST randomized trial, *Eur. Heart J.* 42 (37) (2021) 3844–3852.
- [10] M. Gulati, P.D. Levy, D. Mukherjee, E. Amsterdam, D.L. Bhatt, K.K. Birtcher, R. Blankstein, J. Boyd, R.P. Bullock-Palmer, T. Conejo, D.B. Diercks, F. Gentile, J.P. Greenwood, E.P. Hess, S.M. Hollenberg, W.A. Jaber, H. Jneid, J.A. Joglar, D.A. Morrow, R.E. O'Connor, M.A. Ross, L.J. Shaw, 2021 AHA/ACC/ASE/CHEST/SAEM/SCCT/SCMR guideline for the evaluation and diagnosis of chest pain: Executive summary, *J. Am. Coll. Cardiol.* (2021) <http://dx.doi.org/10.1016/j.jacc.2021.07.052>.
- [11] A. Updegrove, N.M. Wilson, J. Merkow, H. Lan, A.L. Marsden, S.C. Shadden, SimVascular: an open source pipeline for cardiovascular simulation, *Ann. Biomed. Eng.* 45 (2017) 525–541.
- [12] C.A. Taylor, C. Figueroa, Patient-specific modeling of cardiovascular mechanics, *Annu. Rev. Biomed. Eng.* 11 (2009) 109–134.
- [13] C.J. Arthurs, R. Khlebnikov, A. Melville, M. Marčan, A. Gomez, D. Dillon-Murphy, F. Cuomo, M. Silva Vieira, J. Schollenberger, S.R. Lynch, C. Tossas-Betancourt, K. Iyer, S. Hopper, E. Livingston, P. Youssefi, A. Noorani, S. Ben Ahmed, F.J.H. Nauta, T.M.J. van Bakel, Y. Ahmed, P.A.J. van Bakel, J. Mynard, P. Di Achille, H. Gharahi, K.D. Lau, V. Filonova, M. Aguirre, N. Nama, N. Xiao, S. Baek, K. Garikipati, O. Sahni, D. Nordsletten, C.A. Figueroa, CRIMSON: An open-source software framework for cardiovascular integrated modelling and simulation, *PLoS Comput. Biol.* 17 (5) (2021) e1008881.
- [14] R.H. Cox, Wave propagation through a Newtonian fluid contained within a thick-walled, viscoelastic tube, *Biophys. J.* 8 (6) (1968) 691–709.
- [15] C.L. Dumoulin, H. Hart Jr., Magnetic resonance angiography, *Radiology* 161 (3) (1986) 717–720.
- [16] S. Napel, M.P. Marks, G.D. Rubin, M.D. Dake, C.H. McDonnell, S.M. Song, D.R. Enzmann, R. Jeffrey Jr., CT angiography with spiral CT and maximum intensity projection, *Radiology* 185 (2) (1992) 607–610.
- [17] S. Achenbach, W. Moshage, D. Ropers, J. Nossen, W.G. Daniel, Value of electron-beam computed tomography for the noninvasive detection of high-grade coronary-artery stenoses and occlusions, *N. Engl. J. Med.* 339 (27) (1998) 1964–1971.
- [18] C.A. Taylor, T.J. Hughes, C.K. Zarins, Finite element modeling of blood flow in arteries, *Comput. Methods Appl. Mech. Engrg.* 158 (1–2) (1998) 155–196.
- [19] D.A. Steinman, C.A. Taylor, Flow imaging and computing: large artery hemodynamics, *Ann. Biomed. Eng.* 33 (2005) 1704–1709.
- [20] C.A. Taylor, D.A. Steinman, Image-based modeling of blood flow and vessel wall dynamics: applications, methods and future directions, *Ann. Biomed. Eng.* 38 (3) (2010) 1188–1203.
- [21] O. Frank, Die grundform des arteriellen pulses: mathematische analyse. erste abhandlung, 1899.
- [22] T.J. Hughes, J. Lubliner, On the one-dimensional theory of blood flow in the larger vessels, *Math. Biosci.* 18 (1–2) (1973) 161–170.
- [23] D.F. Young, F.Y. Tsai, Flow characteristics in models of arterial stenoses—I. Steady flow, *J. Biomech.* 6 (4) (1973) 395–410.
- [24] M.S. Olufsen, C.S. Peskin, W.Y. Kim, E.M. Pedersen, A. Nadim, J. Larsen, Numerical simulation and experimental validation of blood flow in arteries with structured-tree outflow conditions, *Ann. Biomed. Eng.* 28 (2000) 1281–1299.
- [25] J. Wan, B. Steele, S.A. Spicer, S. Strohband, G.R. Feijóo, T.J. Hughes, C.A. Taylor, A one-dimensional finite element method for simulation-based medical planning for cardiovascular disease, *Comput. Methods Biomech. Biomed. Eng.* 5 (3) (2002) 195–206.
- [26] B.N. Steele, J. Wan, J.P. Ku, T.J. Hughes, C.A. Taylor, In vivo validation of a one-dimensional finite-element method for predicting blood flow in cardiovascular bypass grafts, *IEEE Trans. Biomed. Eng.* 50 (6) (2003) 649–656.
- [27] L. Formaggia, D. Lamponi, A. Quarteroni, One-dimensional models for blood flow in arteries, *J. Eng. Math.* 47 (3–4) (2003) 251–276, <http://dx.doi.org/10.1023/B:ENGL.0000007980.01347.29>, URL <http://infoscience.epfl.ch/record/102952>.
- [28] P. Blanco, S. Watanabe, M. Passos, P. Lemos, R. Feijóo, An anatomically detailed arterial network model for one-dimensional computational hemodynamics, *IEEE Trans. Bio-Med. Eng.* 62 (2014) <http://dx.doi.org/10.1109/TBME.2014.2364522>.
- [29] I.E. Vignon-Clementel, C. Alberto Figueroa, K.E. Jansen, C.A. Taylor, Outflow boundary conditions for three-dimensional finite element modeling of blood flow and pressure in arteries, *Comput. Methods Appl. Mech. Engrg.* 195 (29) (2006) 3776–3796, <http://dx.doi.org/10.1016/j.cma.2005.04.014>, Absorbing Boundary Conditions.
- [30] C.A. Figueroa, I.E. Vignon-Clementel, K.E. Jansen, T.J. Hughes, C.A. Taylor, A coupled momentum method for modeling blood flow in three-dimensional deformable arteries, *Comput. Methods Appl. Mech. Engrg.* 195 (41–43) (2006) 5685–5706.
- [31] N. Xiao, J.D. Humphrey, C.A. Figueroa, Multi-scale computational model of three-dimensional hemodynamics within a deformable full-body arterial network, *J. Comput. Phys.* 244 (2013) 22–40, <http://dx.doi.org/10.1016/j.jcp.2012.09.016>, URL <https://www.sciencedirect.com/science/article/pii/S0021999112005475>, Multi-scale Modeling and Simulation of Biological Systems.
- [32] D. Dillon-Murphy, A. Noorani, D. Nordsletten, C.A. Figueroa, Multi-modality image-based computational analysis of haemodynamics in aortic dissection, *Biomech. Model. Mechanobiol.* 15 (4) (2016) 857–876.

- [33] T.M.J. van Bakel, C.J. Arthurs, F.J.H. Nauta, K.A. Eagle, J.A. van Herwaarden, F.L. Moll, S. Trimarchi, H.J. Patel, C.A. Figueroa, Cardiac remodelling following thoracic endovascular aortic repair for descending aortic aneurysms, *Eur. J. Cardio-Thoracic Surg.* 55 (6) (2018) 1061–1070, <http://dx.doi.org/10.1093/ejcts/ezy399>, arXiv:<https://academic.oup.com/ejcts/article-pdf/55/6/1061/28668043/ezy399.pdf>.
- [34] D. Sengupta, A.M. Kahn, J.C. Burns, S. Sankaran, S.C. Shadden, A.L. Marsden, Image-based modeling of hemodynamics in coronary artery aneurysms caused by kawasaki disease, *Biomech. Model. Mechanobiol.* 11 (6) (2012) 915–932.
- [35] S. Sankaran, M. Esmaily Moghadam, A.M. Kahn, E.E. Tseng, J.M. Guccione, A.L. Marsden, Patient-specific multiscale modeling of blood flow for coronary artery bypass graft surgery, *Ann. Biomed. Eng.* 40 (10) (2012) 2228–2242.
- [36] C.A. Taylor, C.P. Cheng, L.A. Espinosa, B.T. Tang, D. Parker, R.J. Herfkens, In vivo quantification of blood flow and wall shear stress in the human abdominal aorta during lower limb exercise, *Ann. Biomed. Eng.* 30 (2002) 402–408.
- [37] B.T. Tang, C.P. Cheng, M.T. Draney, N.M. Wilson, P.S. Tsao, R.J. Herfkens, C.A. Taylor, Abdominal aortic hemodynamics in young healthy adults at rest and during lower limb exercise: quantification using image-based computer modeling, *Amer. J. Physiol.-Heart Circul. Physiol.* 291 (2) (2006) H668–H676.
- [38] B.T. Tang, T.A. Fonte, F.P. Chan, P.S. Tsao, J.A. Feinstein, C.A. Taylor, Three-dimensional hemodynamics in the human pulmonary arteries under resting and exercise conditions, *Ann. Biomed. Eng.* 39 (2011) 347–358.
- [39] A.S. Les, S.C. Shadden, C.A. Figueroa, J.M. Park, M.M. Tedesco, R.J. Herfkens, R.L. Dalman, C.A. Taylor, Quantification of hemodynamics in abdominal aortic aneurysms during rest and exercise using magnetic resonance imaging and computational fluid dynamics, *Ann. Biomed. Eng.* 38 (2010) 1288–1313.
- [40] G.-Y. Suh, A.S. Les, A.S. Tenforde, S.C. Shadden, R.L. Spilker, J.J. Yeung, C.P. Cheng, R.J. Herfkens, R.L. Dalman, C.A. Taylor, Quantification of particle residence time in abdominal aortic aneurysms using magnetic resonance imaging and computational fluid dynamics, *Ann. Biomed. Eng.* 39 (2011) 864–883.
- [41] K. Perktold, D. Hilbert, Numerical simulation of pulsatile flow in a carotid bifurcation model, *J. Biomed. Eng.* 8 (3) (1986) 193–199.
- [42] L. Formaggia, F. Nobile, A. Quarteroni, A. Veneziani, Multiscale modelling of the circulatory system: a preliminary analysis, *Comput. Vis. Sci.* 2 (1999) 75–83.
- [43] J.B. Keller, D. Givoli, Exact non-reflecting boundary conditions, *J. Comput. Phys.* 82 (1) (1989) 172–192.
- [44] T.J. Hughes, G.R. Feijóo, L. Mazzei, J.-B. Quincy, The variational multiscale method—a paradigm for computational mechanics, *Comput. Methods Appl. Mech. Engrg.* 166 (1–2) (1998) 3–24.
- [45] H. Kim, I. Vignon-Clementel, J. Coogan, C. Figueroa, K. Jansen, C. Taylor, Patient-specific modeling of blood flow and pressure in human coronary arteries, *Ann. Biomed. Eng.* 38 (2010) 3195–3209, <http://dx.doi.org/10.1007/s10439-010-0083-6>.
- [46] K. Menon, J. Seo, R. Fukazawa, S. Ogawa, A.M. Kahn, J.C. Burns, A.L. Marsden, Predictors of myocardial ischemia in patients with Kawasaki disease: Insights from Patient-Specific simulations of coronary hemodynamics, *J. Cardiovasc. Transl. Res.* (2023).
- [47] K.-L.A. Yau, H.J. Lee, Y.-W. Chong, M.H. Ling, A.R. Syed, C. Wu, H.G. Goh, Augmented intelligence: Surveys of literature and expert opinion to understand relations between human intelligence and artificial intelligence, *IEEE Access* 9 (2021) 136744–136761.
- [48] O. Ronneberger, P. Fischer, T. Brox, U-net: Convolutional networks for biomedical image segmentation, in: *Medical Image Computing and Computer-Assisted Intervention—MICCAI 2015: 18th International Conference, Munich, Germany, October 5–9, 2015, Proceedings, Part III* 18, Springer, 2015, pp. 234–241.
- [49] F. Isensee, P.F. Jaeger, S.A. Kohl, J. Petersen, K.H. Maier-Hein, nnU-Net: a self-configuring method for deep learning-based biomedical image segmentation, *Nature Methods* 18 (2) (2021) 203–211, <http://dx.doi.org/10.1038/s41592-020-01008-z>.
- [50] M. Sinclair, A. Schuh, K. Hahn, K. Petersen, Y. Bai, J. Batten, M. Schaap, B. Glocker, Atlas-ISTN: Joint segmentation, registration and atlas construction with image-and-spatial transformer networks, *Med. Image Anal.* 78 (2022) 102383, <http://dx.doi.org/10.1016/j.media.2022.102383>, arXiv:2012.10533.
- [51] I. Laina, N. Rieke, C. Rupprecht, J.P. Vizcaíno, A. Eslami, F. Tombari, N. Navab, Concurrent segmentation and localization for tracking of surgical instruments, in: *Lecture Notes in Computer Science (including subseries Lecture Notes in Artificial Intelligence and Lecture Notes in Bioinformatics)*, in: LNCS, Vol. 10434, 2017, pp. 664–672, arXiv:1703.10701.
- [52] A.F. Frangi, W.J. Niessen, K.L. Vincken, M.A. Viergever, Multiscale vessel enhancement filtering, in: *Medical Image Computing and Computer-Assisted Intervention—MICCAI'98: First International Conference Cambridge, MA, USA, October 11–13, 1998 Proceedings* 1, Springer, 1998, pp. 130–137.
- [53] Y. Tang, D. Yang, W. Li, H.R. Roth, B. Landman, D. Xu, V. Nath, A. Hatamizadeh, Self-supervised pre-training of swin transformers for 3d medical image analysis, in: *Proceedings of the IEEE/CVF Conference on Computer Vision and Pattern Recognition*, 2022, pp. 20730–20740.
- [54] Z. Tu, X. Bai, Auto-context and its application to high-level vision tasks and 3d brain image segmentation, *IEEE Trans. Pattern Anal. Mach. Intell.* 32 (10) (2009) 1744–1757.
- [55] E. Jurrus, A.R. Paiva, S. Watanabe, J.R. Anderson, B.W. Jones, R.T. Whitaker, E.M. Jorgensen, R.E. Marc, T. Tasdizen, Detection of neuron membranes in electron microscopy images using a serial neural network architecture, *Med. Image Anal.* 14 (6) (2010) 770–783.
- [56] M. Seyedhosseini, T. Tasdizen, Semantic image segmentation with contextual hierarchical models, *IEEE Trans. Pattern Anal. Mach. Intell.* 38 (5) (2015) 951–964.
- [57] L.D. Cohen, R. Kimmel, Global minimum for active contour models: A minimal path approach, *Int. J. Comput. Vis.* 24 (1997) 57–78.
- [58] S. Sankaran, H.J. Kim, G. Choi, C.A. Taylor, Uncertainty quantification in coronary blood flow simulations: impact of geometry, boundary conditions and blood viscosity, *J. Biomech.* 49 (12) (2016) 2540–2547.
- [59] D. Lesage, E.D. Angelini, I. Bloch, G. Funka-Lea, A review of 3D vessel lumen segmentation techniques: Models, features and extraction schemes, *Med. Image Anal.* 13 (6) (2009) 819–845.

- [60] K. Uzu, H. Otake, G. Choi, T. Toba, H.J. Kim, A. Roy, M. Schaap, L. Grady, M. Kawata, T. Shinke, et al., Lumen boundaries extracted from coronary computed tomography angiography on computed fractional flow reserve (FFRCT): validation with optical coherence tomography, *Eurointervention: J. Europer Collab. Work. Group Interv. Cardiol. Eur. Soc. Cardiol.* 14 (15) (2019) e1609–e1618.
- [61] A. Kanitsar, D. Fleischmann, R. Wegenkittl, P. Felkel, E. Groller, CPR-Curved Planar Reformation, *IEEE*, 2002.
- [62] O. Sahni, J. Müller, K.E. Jansen, M.S. Shephard, C.A. Taylor, Efficient anisotropic adaptive discretization of the cardiovascular system, *Comput. Methods Appl. Mech. Engrg.* 195 (41–43) (2006) 5634–5655.
- [63] O. Sahni, K.E. Jansen, M.S. Shephard, C.A. Taylor, M.W. Beall, Adaptive boundary layer meshing for viscous flow simulations, *Eng. Comput.* 24 (2008) 267–285.
- [64] Simmetrix, Meshsim, 2023, URL <http://www.simmetrix.com/>.
- [65] M. Esmaily Moghadam, Y. Bazilevs, T.-Y. Hsia, I.E. Vignon-Clementel, A.L. Marsden, A comparison of outlet boundary treatments for prevention of backflow divergence with relevance to blood flow simulations, *Comput. Mech.* 48 (3) (2011) 277–291.
- [66] C.H. Whiting, K.E. Jansen, A stabilized finite element method for the incompressible Navier–Stokes equations using a hierarchical basis, *Internat. J. Numer. Methods Fluids* 35 (2001) 93–116.
- [67] M. Esmaily-Moghadam, Y. Bazilevs, A.L. Marsden, A bi-partitioned iterative algorithm for solving linear systems arising from incompressible flow problems, *Comput. Methods Appl. Mech. Engrg.* 286 (2015) 40–62, <http://dx.doi.org/10.1016/j.cma.2014.11.033>, URL <https://www.sciencedirect.com/science/article/pii/S0045782514004666>.
- [68] A.N. Brooks, T.J. Hughes, Streamline upwind/Petrov-Galerkin formulations for convection dominated flows with particular emphasis on the incompressible Navier-Stokes equations, *Comput. Methods Appl. Mech. Engrg.* 32 (1) (1982) 199–259, [http://dx.doi.org/10.1016/0045-7825\(82\)90071-8](http://dx.doi.org/10.1016/0045-7825(82)90071-8).
- [69] L.P. Franca, S.L. Frey, Stabilized finite element methods: II. The incompressible Navier-Stokes equations, *Comput. Methods Appl. Mech. Engrg.* 99 (2) (1992) 209–233, [http://dx.doi.org/10.1016/0045-7825\(92\)90041-H](http://dx.doi.org/10.1016/0045-7825(92)90041-H).
- [70] L.M. Itu, P. Sharma, V. Mihalef, A. Kamen, C. Suciu, D. Lomaniciu, A patient-specific reduced-order model for coronary circulation, in: *Proceedings / IEEE International Symposium on Biomedical Imaging: from nano to macro. IEEE International Symposium on Biomedical Imaging*, 2012, pp. 832–835, <http://dx.doi.org/10.1109/ISBI.2012.6235677>.
- [71] J.P. Mynard, K. Valen-Sendstad, A unified method for estimating pressure losses at vascular junctions, *Int. J. Numer. Methods Biomed. Eng.* 31 (2015) URL <https://api.semanticscholar.org/CorpusID:205686481>.
- [72] P. Blanco, C. Bulant, L. Mueller, G. Maso Talou, C. Bezerra, P. Lemos, R. Feijóo, Comparison of 1D and 3D models for the estimation of fractional flow reserve, *Sci. Rep.* 8 (2018) <http://dx.doi.org/10.1038/s41598-018-35344-0>.
- [73] M. Mirramezani, S.C. Shadden, A distributed lumped parameter model of blood flow, *Ann. Biomed. Eng.* 48 (2020) 2870–2886, <http://dx.doi.org/10.1007/s10439-020-02545-6>.
- [74] K.G. Lyras, J. Lee, An improved reduced-order model for pressure drop across arterial stenoses, *PLoS One* 16 (10) (2021) 1–22, <http://dx.doi.org/10.1371/journal.pone.0258047>.
- [75] F.E. Fossan, L.O. Müller, J. Sturdy, A.T. Bråten, A. Jørgensen, R. Wiseth, L.R. Hellevik, Machine learning augmented reduced-order models for FFR-prediction, *Comput. Methods Appl. Mech. Engrg.* 384 (2021) <http://dx.doi.org/10.1016/j.cma.2021.113892>.
- [76] S. Sankaran, D. Lesage, R. Tombropoulos, N. Xiao, H.J. Kim, D. Spain, M. Schaap, C.A. Taylor, Physics driven real-time blood flow simulations, *Comput. Methods Appl. Mech. Engrg.* 364 (2020) 112963, <http://dx.doi.org/10.1016/j.cma.2020.112963>, URL <https://www.sciencedirect.com/science/article/pii/S0045782520301468>.
- [77] J.S. Choy, G.S. Kassab, Scaling of myocardial mass to flow and morphometry of coronary arteries, *J. Appl. Physiol.* 104 (5) (2008) 1281–1286, <http://dx.doi.org/10.1152/japplphysiol.01261.2007>.
- [78] R.F. Wilson, K. Wyche, B.V. Christensen, S. Zimmer, D.D. Laxson, Effects of adenosine on human coronary arterial circulation, *Circulation* 82 (5) (1990) 1595–1606.
- [79] K.L. Gould, K. Lipscomb, Effects of coronary stenoses on coronary flow reserve and resistance, *Amer. J. Cardiol.* 34 (1) (1974) 48–55, [http://dx.doi.org/10.1016/0002-9149\(74\)90092-7](http://dx.doi.org/10.1016/0002-9149(74)90092-7).
- [80] L.O. Müller, F.E. Fossan, A.T. Bråten, A. Jørgensen, R. Wiseth, L.R. Hellevik, Impact of baseline coronary flow and its distribution on fractional flow reserve prediction, *Int. J. Numer. Methods Biomed. Eng.* 37 (11) (2021) e3246.
- [81] R. Nakazato, H.-B. Park, D.S. Berman, H. Gransar, B.-K. Koo, A. Erglis, F.Y. Lin, A.M. Dunning, M.J. Budoff, J. Malpeso, et al., Noninvasive fractional flow reserve derived from computed tomography angiography for coronary lesions of intermediate stenosis severity: results from the DeFACTO study, *Circul.: Cardiovasc. Imaging* 6 (6) (2013) 881–889.
- [82] T.A. Fairbairn, K. Nieman, T. Akasaka, B.L. Nørgaard, D.S. Berman, G. Raff, L.M. Hurwitz-Koweeck, G. Pontone, T. Kawasaki, N.P. Sand, et al., Real-world clinical utility and impact on clinical decision-making of coronary computed tomography angiography-derived fractional flow reserve: lessons from the ADVANCE registry, *Eur. Heart J.* 39 (41) (2018) 3701–3711.
- [83] M.R. Patel, B.L. Nørgaard, T.A. Fairbairn, K. Nieman, T. Akasaka, D.S. Berman, G.L. Raff, L.M. Hurwitz Koweeck, G. Pontone, T. Kawasaki, et al., 1-year impact on medical practice and clinical outcomes of FFRCT: the ADVANCE registry, *Cardiovasc. Imaging* 13 (1\_Part\_1) (2020) 97–105.
- [84] M.G. Nanna, S. Vemulapalli, C.B. Fordyce, D.B. Mark, M.R. Patel, H.R. Al-Khalidi, M. Kelsey, B. Martinez, E. Yow, S. Mullen, et al., The prospective randomized trial of the optimal evaluation of cardiac symptoms and revascularization: Rationale and design of the PRECISE trial, *Amer. Heart J.* 245 (2022) 136–148.
- [85] P.S. Douglas, M.G. Nanna, M.D. Kelsey, E. Yow, D.B. Mark, M.R. Patel, C. Rogers, J.E. Udelson, C.B. Fordyce, N. Curzen, et al., Comparison of an initial risk-based testing strategy vs usual testing in stable symptomatic patients with suspected coronary artery disease: the PRECISE randomized clinical trial, *JAMA Cardiol.* (2023).
- [86] J.M. Lee, G. Choi, B.-K. Koo, D. Hwang, J. Park, J. Zhang, K.-J. Kim, Y. Tong, H.J. Kim, L. Grady, et al., Identification of high-risk plaques destined to cause acute coronary syndrome using coronary computed tomographic angiography and computational fluid dynamics, *Cardiovasc. Imaging* 12 (6) (2019) 1032–1043.



- [87] S. Yang, G. Choi, J. Zhang, J.M. Lee, D. Hwang, J.-H. Doh, C.-W. Nam, E.-S. Shin, Y.-S. Cho, S.-Y. Choi, et al., Association among local hemodynamic parameters derived from CT angiography and their comparable implications in development of acute coronary syndrome, *Front. Cardiovasc. Med.* 8 (2021) 713835.
- [88] S.H. Lee, D. Hong, N. Dai, D. Shin, K.H. Choi, S.M. Kim, H.K. Kim, K.-H. Jeon, S.J. Ha, K.Y. Lee, et al., Anatomic and hemodynamic plaque characteristics for subsequent coronary events, *Front. Cardiovasc. Med.* 9 (2022) 871450.
- [89] S. Sankaran, D. Lesage, R. Tombropoulos, N. Xiao, H.J. Kim, D. Spain, M. Schaap, C.A. Taylor, Physics driven real-time blood flow simulations, *Comput. Methods Appl. Mech. Engrg.* 364 (2020) 112963.
- [90] J. Sonck, S. Nagumo, B.L. Norgaard, H. Otake, B. Ko, J. Zhang, T. Mizukami, M. Maeng, D. Andreini, Y. Takahashi, et al., Clinical validation of a virtual planner for coronary interventions based on coronary CT angiography, *Cardiovasc. Imaging* 15 (7) (2022) 1242–1255.
- [91] D. Andreini, C. Collet, J. Leipsic, K. Nieman, M. Bittencurt, J. De Mey, N. Buls, Y. Onuma, S. Mushtaq, E. Conte, et al., Pre-procedural planning of coronary revascularization by cardiac computed tomography: An expert consensus document of the society of cardiovascular computed tomography, *J. Cardiovasc. Comput. Tomogr.* 16 (6) (2022) 558–572.
- [92] C. Collet, J. Sonck, J. Leipsic, G. Monizzi, D. Buytaert, P. Kitslaar, D. Andreini, B. De Bruyne, Implementing coronary computed tomography angiography in the catheterization laboratory, *Cardiovasc. Imaging* 14 (9) (2021) 1846–1855.
- [93] C. Collet, Y. Onuma, D. Andreini, J. Sonck, G. Pompilio, S. Mushtaq, M. La Meir, Y. Miyazaki, J. de Mey, O. Gaemperli, et al., Coronary computed tomography angiography for heart team decision-making in multivessel coronary artery disease, *Eur. Heart J.* 39 (41) (2018) 3689–3698.
- [94] S. Sankaran, M. Esmaily Moghadam, A.M. Kahn, E.E. Tseng, J.M. Guccione, A.L. Marsden, Patient-specific multiscale modeling of blood flow for coronary artery bypass graft surgery, *Ann. Biomed. Eng.* 40 (2012) 2228–2242.
- [95] A. Lin, N. Manral, P. McElhinney, A. Killekar, H. Matsumoto, J. Kwiecinski, K. Pieszko, A. Razipour, K. Grodecki, C. Park, et al., Deep learning-enabled coronary CT angiography for plaque and stenosis quantification and cardiac risk prediction: an international multicentre study, *Lancet Digit. Health* 4 (4) (2022) e256–e265.
- [96] J. Narula, T. Stuckey, G. Nakazawa, A. Maehara, M. Matsumura, K. Petersen, S. Mirza, N. Ng, S. Mullen, M. Schaap, et al., Primary results of the revealplaque study: A prospective quantitative assessment of AI-based CCTA plaque volume compared with IVUS, *J. Cardiovasc. Comput. Tomogr.* 17 (4) (2023) S39.
- [97] M.R. Patel, E.D. Peterson, D. Dai, J.M. Brennan, R.F. Redberg, H.V. Anderson, R.G. Brindis, P.S. Douglas, Low diagnostic yield of elective coronary angiography, *N. Engl. J. Med.* 362 (10) (2010) 886–895, <http://dx.doi.org/10.1056/nejmoa0907272>.
- [98] F.J. Neumann, U. Sechtem, A.P. Banning, N. Bonaros, H. Bueno, R. Bugiardini, A. Chieffo, F. Crea, M. Czerny, V. Delgado, P. Dendale, J. Knuuti, W. Wijns, F.A. Flachskampf, H. Gohlke, E.L. Grove, S. James, D. Katritsis, U. Landmesser, M. Lettino, C.M. Matter, H. Nathoe, A. Niessner, C. Patrono, A.S. Petronio, S.E. Pettersen, R. Piccolo, M.F. Piepoli, B.A. Popescu, L. Räber, D.J. Richter, M. Roffi, F.X. Roithinger, E. Shlyakhto, D. Sibbing, S. Silber, I.A. Simpson, M. Sousa-Uva, P. Vardas, A. Witkowski, J.L. Zamorano, S. Achenbach, S. Agewall, E. Barbato, J.J. Bax, D. Capodanno, T. Cuisset, C. Deaton, K. Dickstein, T. Edvardsen, J. Escaned, C. Funck-Brentano, B.J. Gersh, M. Gilard, D. Hasdai, R. Hatala, F. Mahfoud, J. Masip, C. Muneretto, E. Prescott, A. Saraste, R.F. Storey, P. Svitil, M. Valgimigli, V. Aboyans, C. Baigent, J.P. Collet, V. Dean, D. Fitzsimons, C.P. Gale, D.E. Grobbee, S. Halvorsen, G. Hindricks, B. Iung, P. Jüni, H.A. Katus, C. Leclercq, B.S. Lewis, B. Merkely, C. Mueller, S. Petersen, R.M. Touyz, S. Benkhedda, B. Metzler, V. Sujayeva, B. Cosyns, Z. Kusljagic, V. Velchev, G. Panayi, P. Kala, S.A. Haahr-Pedersen, H. Kabil, T. Ainala, T. Kaukonen, G. Cayla, Z. Pagava, J. Woehrle, J. Kanakakis, K. Toth, T. Gudnason, A. Peace, D. Aronson, C. Riccio, S. Elezi, E. Mirzakhimov, S. Hansone, A. Sarkis, R. Babarskiene, J. Beissel, A.J. Cassar Maempel, V. Revenco, G.J. de Grooth, H. Pejkov, V. Juliebø, P. Lipiec, J. Santos, O. Chioncel, D. Duplyakov, L. Bertelli, A.D. Dikic, M. Studencan, M. Bunc, F. Alfonso, M. Back, M. Zellweger, F. Addad, A. Yildirim, Y. Sirenko, B. Clapp, 2019 ESC guidelines for the diagnosis and management of chronic coronary syndromes, 2020, <http://dx.doi.org/10.1093/eurheartj/ehz425>.
- [99] G. Toth, M. Hamilos, S. Pyxaras, F. Mangiacapra, O. Nelis, F. De Vroey, L. Di Serafino, O. Muller, C. Van Mieghem, E. Wyffels, et al., Evolving concepts of angiogram: fractional flow reserve discordances in 4000 coronary stenoses, *Eur. Heart J.* 35 (40) (2014) 2831–2838.
- [100] C.A. Taylor, S. Gaur, J. Leipsic, S. Achenbach, D.S. Berman, J.M. Jensen, D. Dey, H.E. Bøtker, H.J. Kim, S. Khem, et al., Effect of the ratio of coronary arterial lumen volume to left ventricle myocardial mass derived from coronary CT angiography on fractional flow reserve, *J. Cardiovasc. Comput. Tomogr.* 11 (6) (2017) 429–436.
- [101] W.F. Fearon, L.B. Balam, H.M. Farouque, R.C. Robbins, P.J. Fitzgerald, P.G. Yock, A.C. Yeung, Novel index for invasively assessing the coronary microcirculation, *Circulation* 107 (25) (2003) 3129–3132, <http://dx.doi.org/10.1161/01.CIR.0000080700.98607.D1>.
- [102] B. De Bruyne, N.H. Pijls, E. Gallinoro, A. Candrea, S. Fournier, D.C. Keulards, J. Sonck, M. van't Veer, E. Barbato, J. Bartunek, M. Vanderheyden, E. Wyffels, A. De Vos, M. El Farissi, P.A. Tonino, O. Muller, C. Collet, W.F. Fearon, Microvascular resistance reserve for assessment of coronary microvascular function: JACC technology corner, *J. Am. Coll. Cardiol.* 78 (15) (2021) 1541–1549, <http://dx.doi.org/10.1016/j.jacc.2021.08.017>.
- [103] C.K.M. Boerhout, J.M. Lee, G.A. de Waard, H. Mejia-Renteria, S.H. Lee, J.-h. Jung, M. Hoshino, M. Echavarria-Pinto, M. Meuwissen, H. Matsuo, M. Madera-Cambero, A. Eftekhari, M.A. Effat, T. Murai, K. Marques, J.-h. Doh, E.H. Christiansen, R. Banerjee, C.-w. Nam, G. Niccoli, M. Nakayama, N. Tanaka, E.-s. Shin, Y. Appelman, M.A.M. Beijik, N. van Royen, P. Knaapen, J. Escaned, T. Kakuta, B.K. Koo, J.J. Piek, T.P. van de Hoef, Microvascular resistance reserve: diagnostic and prognostic performance in the ILIAS registry, *Eur. Heart J.* (2023) 1–8, <http://dx.doi.org/10.1093/eurheartj/ehad378>.
- [104] C. Jaquet, L. Najman, H. Talbot, L. Grady, M. Schaap, B. Spain, H.J. Kim, I. Vignon-Clementel, C.A. Taylor, Generation of patient-specific cardiac vascular networks: A hybrid image-based and synthetic geometric model, *IEEE Trans. Biomed. Eng.* 66 (4) (2019) 946–955, <http://dx.doi.org/10.1109/TBME.2018.2865667>.



- [105] S. Di Gregorio, M. Fedele, G. Pontone, A.F. Corno, P. Zunino, C. Vergara, A. Quarteroni, A computational model applied to myocardial perfusion in the human heart: From large coronaries to microvasculature, *J. Comput. Phys.* 424 (2021) 109836, <http://dx.doi.org/10.1016/j.jcp.2020.109836>.
- [106] H.J. Kim, H.C. Rundfeldt, I. Lee, S. Lee, Tissue-growth-based synthetic tree generation and perfusion simulation, 2023, <http://dx.doi.org/10.1007/s10237-023-01703-8>.
- [107] L. Papamanolis, H.J. Kim, C. Jaquet, M. Sinclair, M. Schaap, I. Danad, P. van Diemen, P. Knaapen, L. Najman, H. Talbot, C.A. Taylor, I. Vignon-Clementel, Myocardial perfusion simulation for coronary artery disease: A coupled patient-specific multiscale model, *Ann. Biomed. Eng.* 49 (5) (2021) 1432–1447, <http://dx.doi.org/10.1007/s10439-020-02681-z>.
- [108] R. Chabiniok, V.Y. Wang, M. Hadjicharalambous, L. Asner, J. Lee, M. Sermesant, E. Kuhl, A.A. Young, P. Moireau, M.P. Nash, D. Chapelle, D.A. Nordsletten, Multiphysics and multiscale modelling, data-model fusion and integration of organ physiology in the clinic: ventricular cardiac mechanics, *Interface Focus* 6 (2) (2016) 20150083, <http://dx.doi.org/10.1098/rsfs.2015.0083>.
- [109] M. Peirlinck, F.S. Costabal, J. Yao, J.M. Guccione, S. Tripathy, Y. Wang, D. Ozturk, P. Segars, T.M. Morrison, S. Levine, E. Kuhl, Precision medicine in human heart modeling, *Biomech. Model. Mechanobiol.* (0123456789) (2021) <http://dx.doi.org/10.1007/s10237-021-01421-z>.
- [110] M. Fedele, R. Piersanti, F. Regazzoni, M. Salvador, P.C. Africa, M. Bucelli, A. Zingaro, A. Quarteroni, et al., A comprehensive and biophysically detailed computational model of the whole human heart electromechanics, *Comput. Methods Appl. Mech. Engrg.* 410 (2023) 115983.
- [111] C.A. Taylor, M.T. Draney, J.P. Ku, D. Parker, B.N. Steele, K. Wang, C.K. Zarins, Predictive medicine: computational techniques in therapeutic decision-making, *Comput. Aided Surg.: Off. J. Int. Soc. Comput. Aided Surg. (ISCAS)* 4 (5) (1999) 231–247.